RESEARCH ARTICLE

NANO · MICRO small
www.small-journal.com

Flexible MXene/Laser-Induced Porous Graphene Asymmetric Supercapacitors: Enhanced Energy Density of Lateral and Sandwich Architectures Under Different Electrolytes

Sanju Gupta, Magdalena Narajczyk, Mirosław Sawczak, Jacek B. Jasinski, Robert Bogdanowicz, and Shubin Yang*

Deployment of 2D layered materials beyond graphene, i.e., MXene ($Ti_3C_2T_x$, T = —OH, F, O) is rigorously explored for generation-II electrochemical energy storage systems. The strategic development of asymmetric supercapacitors (ASCs) comprising MXene as negative and laser—induced porous graphene (LIPG) as a positive electrode (i.e., MXene//LIPG) is reported to improve electrochemical energy storage in lateral (coplanar) and sandwich (cofacial) device configurations. Moreover, the interdigitated lateral device is scalable, flexible, current—collector, and binder-free. Electrochemical performance is evaluated under various electrolyte compositions: aqueous (AE), organic (OE), and ionic liquid (ILE). Notably, ASCs operate up to ≈1.0 V with AE, 1.6—2.0 V with OE, and 2.4—3.0 V with ILE exhibit enhanced energy densities depending upon the electrolyte and 100% Coulombic efficiency while retaining 75–95 % of initial capacitance after thousands of cycles (≥10 000–200 000). Specifically, the highest specific energy density (289 mW h cm^{-3} at power density 0.2 W cm^{-3}) is recorded for ILE-sandwich, seven times higher as compared with AE-sandwich (40 mW h cm^{-3} at power density 0.4 W cm^{-3}) followed by intermediate value for OE-lateral (8.5 mW h cm^{-3} at power density 0.14 W cm^{-3}) device. On the other hand, symmetric (MXene//MXene) device provided for sandwich (ILE: 12 W h cm^{-3} at power density 0.5 W cm^{-3}; OE: 8.8 mW h cm^{-3} at power density 0.1 W cm^{-3}, AE: 4.2 mW h cm^{-3} at power density 0.1 W cm^{-3}) and lateral (OE: 3 mW h cm^{-3} at power density 0.2 W cm^{-3}) configurations. Experimental findings are discussed within the framework of novel and constructive dual functionality of asymmetric electrodes' charging mechanism offer a benchmark for high-performing next-generation flexible microscale supercapacitors.

1. Introduction

Global demand for electric energy due to industrialization has prompted rapid increase in energy production from sustainable sources.[1] One of the renewable energy sources is the electricity production from solar energy by photovoltaics provide a significant part of electricity requirements. Electrochemical energy conversion and storage (EECS) systems such as electrochemical capacitors, rechargeable secondary, and redox flow batteries represent the most environmentally benign continual technologies[2–4], and currently, they are central to the modern renewable energy landscape for power—hungry applications.[5–7] Research efforts so far have concentrated primarily on electrochemical capacitors (generation-I supercapacitors) due to their satisfactory characteristics of rapid high-power supply (discharge), storage of electricity (charge), and extended lifetime in contrast to batteries recognized for their high energy capacity with limited shelf life.[8–10] However, neither the batteries nor supercapacitors alone satisfy current energy needs.[11] In the supercapacitor, the charge storage originates from the electric double-layer (EDLC), whereas pseudocapacitance is associated

The ORCID identification number(s) for the author(s) of this article can be found under https://doi.org/10.1002/smll.202502297

DOI: 10.1002/smll.202502297

S. Gupta, R. Bogdanowicz
Department of Metrology and Optoelectronics
Faculty of Electronics
Telecommunication and Informatics, Gdańsk University of Technology
Narutowicza Str. 11/12, Gdańsk 80-233, Poland
E-mail: sangupta@pg.edu.pl

with the faradaic reaction of redox-active species from electrolyte or electrode material leading to higher energy density.[12–15] The ability to accept full recharge in a short time is desirable in energy sources for uninterrupted power supply and automotive applications.[16–18] Typically, the efficiency of EECS depends upon a variety of factors include, the chemical composition of electrodes, electrochemical environment (electrolyte) driving the surface redox and bulk intercalation chemistry, as well as device architectures.[19,20] Therefore, to improve energy density using strategic combination of electrodes and device configurations (*e.g.*, sandwich or cofacial and lateral or coplanar) influencing dynamic energy storage tuned delicately for each application has been the driving force to develop generation−II electrochemical energy storage systems that can offer comparable performance to batteries at affordable cost.[21–23]

The novel electrode formulations enabled by nanotechnology provide indispensable benefits by synergistic combination of chemical and physical properties (*e.g.*, specific surface area, electrical conductivity, mechanically robust framework, thermal and chemical stability) to realize commercially relevant specific energy and power density capabilities to advance along the Ragone plot diagonally.[24] Typical electrochemical electrodes (supercapacitive cathodes[19,25] and battery anodes[26,27]) materials include carbonaceous, two-and 3D graphene nanomaterials[28] giving rise to exceptional electronic and thermal conductivity, electroactivity, higher specific surface area (≈2,630 m^2g^{-1}), low density, mechanical robustness, and long−life cyclability/stability under various electrochemical environment[29–33] Other morphologically diverse carbons assessed are vertically aligned graphene or carbon nanowalls (G/CNWs),[34] graphene aerogels (GAs), and mesoporous graphene.[35–37] Interestingly, while multiplexed graphene nanosheets enhanced specific surface area, the low pore wall thickness in nanoporous carbons is believed to decrease the electronic density of states near the Fermi level, which in turn limits the total interfacial capacitance affecting energy storage capacity. Among these efforts, the scope of the graphene family is expanded by introducing novel laser-induced 'porous' graphene (LIPG). It is a 3D-interconnected network of graphene nanosheets forming macroporous film produced through a scalable, industrially deployable, single-step infrared laser manufacturing technique on commercial polyimide (PI) film as an ideal carbon source, favorable for customizable devices.[38–40] Despite being a relatively new addition to graphene-family nanomaterials, the use of 2D graphene material in 3D (3D) superstructures inspired flexible and foldable micro-supercapacitors (MSCs), and applications in life sciences, biochemical sensors, and environmental remediation.[41–43] Furthermore, rapid deployment of layered materials beyond graphene includes carbide-derived carbons, also called MXenes (*e.g.*, T_x−terminated $Ti_3C_2T_x$) that has been rigorously explored besides metal oxides,[44–46] conducting polymers,[47,48] transition metal dichalcogenides,[49–51] and metal-organic frameworks behaving as pseudocapacitive cathodes[52] for generation-II EECS.[53–55] The persistent interest in nanostructured layered materials arises due to structural polymorphism, chemical stability, rich surface chemistry in addition to a variety of physical and chemical processes that are deeply associated with electrochemical environment such as wide operating potential window in organic and ionic liquid electrolytes, addressed in this work[56–58] Among the electrolytes used are aqueous electrolytes, AE (*e.g.*, KOH, H_2SO_4, Na_2SO_4) for easier ionic conduction, cost, and safety (non-inflammable), despite limited in operating voltage ≈1.0 V due to electrolysis (≈1.23 V).[59] Organic electrolyte (OE) in the form of polymer gel that exhibit lower conductivity and ion mobility, which can decrease power density, however, they demonstrate smaller self-discharge. Though it is worth pointing out that polymer gel or organic electrolytes (polyvinyl alcohol, PVA with H_2SO_4)[60,21] are well suited for flexible printed energy storage devices and can operate in larger potential windows (≈2V). On the other hand, room temperature ionic liquid electrolytes (ILE) consisting of large ion sizes free of molecular solvent emerged as a greener alternative due to high thermal stability, low volatility, non-flammability, extreme electrochemical stability (a wide potential window identified up to 5V), and tunable polarity.[61,62] ILE based on 1-ethyl-3-methylimidazolium cation and trifluoromethylsulfonyl imide anion ([EMIM][TFSI]) is known to possess desirable characteristics, however, due to higher viscosity, they are occasionally mixed with acetonitrile (AN) or propylene carbonate (PC) without declining ionic conductivity.

This work reports the strategic design and development of asymmetric supercapacitors (ASCs) through a combination of MXene as the negative electrode and LIPG as the positive electrode. The two dissimilar electrodes exhibit different charge storage mechanisms, pseudocapacitive (MXene) and EDLC(LIPG), in which larger operating potential windows and enhanced specific energy density are realized, compared to symmetric (MXene) supercapacitors.[63] Typically for such ASCs, carbon nanomaterials as anode and transition metal oxides as cathodes are utilized. However, some metal oxides/nitrides and MXene can work in a negative potential due to the nature of oxidation since degradation occurs at positive potentials, as adopted in this study. Given that MXene performs admirably in all electrolyte media, the MXene//LIPG device performance is conducted under three electrolyte compositions. Furthermore, the miniaturization of electronic devices and the emergence of smart autonomous

S. Gupta, R. Bogdanowicz
Advanced Materials Center
Gdańsk University of Technology
Gdańsk 80-233, Poland

S. Gupta
Department of Physics
Pennsylvania State University
University Park, PA 16802, USA

M. Narajczyk
Faculty of Biology
Bioimaging Laboratory
University of Gdansk
Wita Stwosza 59, Gdańsk 80-308, Poland

M. Sawczak
The Szewalski Institute of Fluid-Flow Machinery
Polish Academy of Sciences
Fiszera 14, Gdańsk 80-231, Poland

J. B. Jasinski
Conn Center for Renewable Energy Research
University of Louisville
Louisville, KY 40292, USA

S. Yang
School of Materials Science and Engineering
Beihang University
Beijing 100191, China

systems require the development of on-chip storage solutions. Currently, thin-film or micro-batteries used for small-scale energy storage often suffer from low power density and limited cycle-life.[64] As a result, we developed flexible micro-supercapacitors in lateral (*coplanar*) and sandwich (*cofacial*) configurations as stand-alone energy sources that could provide the required power to microsensors and nanorobots. We report a facile approach to produce microscale ASCs which is scalable, current−collector, and binder-free in contrast to current fabrication methods often involve multistep processing and time−consuming lithography protocols. In this study, the unprecedented experimental findings are discussed in terms of constructive dual functionality of asymmetric electrode component charging mechanisms leading to enhanced specific energy density while advancing our understanding of dynamic electrified interfaces under various environments and establishing the next generations of electrochemical energy device roadmap.

2. Results and Discussion

2.1. Morphology and Microstructure of LIPG and MXene Electrodes

We characterized the constituent electrode materials for their surface morphology and microstructure prior to electrochemical properties revealing characteristic features associated with complex LIPG and MXene electrodes. The laser-induced porous graphene on PI polymer film paved the way toward scalable production for flexible micro-supercapacitors illustrated in **Figure 1** (panel a).[65] Commercial PI film is an ideal carbon precursor containing aromatic (cyclic) and imide (NH^{2-}) repeat units, in contrast to aliphatic chains, that undergo depolymerization at laser-induced temperatures for producing continuous 3D multilayer graphene films efficiently.[66] In general, the underlying mechanism of a single-pass chemical-free synthesis method involves carbonization on PI surface under infrared CO_2 laser scribing which photothermally dissociates C—O, C═O, and N–C bonds and leads to C—C recombination resulting in the conversion of sp^3–carbon (sp^3 C) atoms to sp^2–carbon (sp^2 C) atoms.[51] Moreover, the rapid liberation of carbonaceous and nitric gases from PI melt gives rise to formation of 3D porous networked graphenic structures. The LIPG consists of hexagon structural motifs besides pentagon−heptagon and occassional octagon coordinated rings as dominant defect structures favorable for accessing electrolyte ions and modifying electroactivity. On the other hand, 2D layered MXene was synthesized using the process described in Figure 1b, i.e., by selective etching of Al layer from MAX phase followed by freeze-dry to prepare monolithic 'cakes' of MXene layers that are re-dispersible in water.

Figure 1c–f show representative micrographs of LIPG and MXene specimen at microscale (SEM) and nanoscale (TEM) revealing surface morphology and internal structure. LIPG shows 3D multiplexed graphitic nanosheet web appearing as "soap bubble" foam with porous structures resulting from a rapid liberation of gas and corrugated surface morphology with occasional amorphous carbon (*a*−C). These porous structures render enhanced-accessible surface area and facilitate electrolyte confinement when used as active electrode material. Some of the images are falsely colored to emphasize 'accordion-like' layered structure morphology. The layers also exhibit intrinsic microscopic roughening and surface corrugations such that out-of-plane deformation ≈1 nm exists and consists of folded edges like graphene nanosheets. The high-resolution TEM images of MXene indicate layer thickness from one to a few nanometers. Also shown are the selected area electron diffraction (SAED) of LIPG with continuous rings indicative of disordered structure and MXene with a well-defined pattern demonstrating crystallinity. MXene phase is evidenced by hexagonal symmetry spots and the anatase TiO_2 phase is confirmed by the appearance of diffraction rings revealing a polycrystalline phase (Figure 1h) with medium- to long-range order. The c-lattice parameter and interlayer distance are 3.46, 21.6 Å (22.6, 12.4 Å) for LIPG (MXene), respectively.

The XRD spectra in Figure 1i result from the LIPG electrode film along with precursor PI and MXene film in 2θ range from 5° to 70°. The crystallite size along the *c* axis (d_c) and domain size in *a* axis (d_a) of LIPG is calculated using Equations (1) and (2), respectively:

$$d_c = \frac{0.89\lambda}{\beta_{hkl} cos\theta_{hkl}} \quad (1)$$

$$d_a = \frac{1.84\lambda}{\beta_{hkl} cos\theta_{hkl}} \quad (2)$$

where λ (= 1.54 Å) is X-ray wavelength and β_{hkl} (in radian units) is peak full width at half maximum. The XRD pattern of LIPG shows a major diffraction peak centered at $2\theta = 25.2°$ giving an interlayer spacing (d_c) of ≈3.62 Å between (002) graphene planes, indicative of a high degree of graphitization. The asymmetry of (002) peak points to an increased I_c. The expanded d_c is attributed to regions where defects are distributed on hexagonal graphene layers. The peak at $2\theta = 42.5°$ indexed to (100) reflection is associated with an in-plane structure. Using Equations (1) and (2), the crystalline size along *c* and *a* axis is calculated to be ≈18 and ≈34 nm, respectively. The MXene sample reveals characteristic sharp peaks associated with MXene phases of rhombohedral graphite (ICDD 01-075-2078) and hexagonal $Ti_3AlC_2T_x$ (ICDD 00-052-0875). It is evident that the $Ti_3C_2T_x$ (MXene) nanosheets are well dispersed and samples are well-crystalized.[67] Peaks at 2θ = 9.8, 18.3, 27.5, 34.1, 36.2, 39.0, 41.7, 50.8 and 52.7° are assigned to (002), (004), (006), (008), (101), (103), (104), (105), (107) and (108) planes, respectively. Among these, (004), (006), (008), and (105) indicate MXene phase, while other crystal planes are present due to Ti_3AlC_2. The absence of a sharp peak at 2θ ≈25° corresponding to (101) plane of anatase TiO_2 implies no reductivity in MXene dispersion. The formation of Ti_3C_2 phase in XRD pattern instead of $Ti_3C_2(OH)_2$ is because the ultrasonication leads to the exfoliation of MXene Ti_3C_2 phase.[68] The delaminating and exfoliating processes verified by XRD involve the etching away of Al from Ti_3AlC_2 revealed by the vanishing of (104) peak at 39°. Moreover, the broader peak suggests its origin from less regular structures, Ti3C2Tx nanosheets loosely stacked with each other via van der Walls interactions. Concomitantly, the (002) diffraction peak at 9.8° and 27.5° angles confirm the delamination process since Al is replaced by OH and F yielding interplanar spacing of 9.02 and 3.32 Å. Figure 1j shows micro-Raman spectra of LIPG and MXene electrode films. They

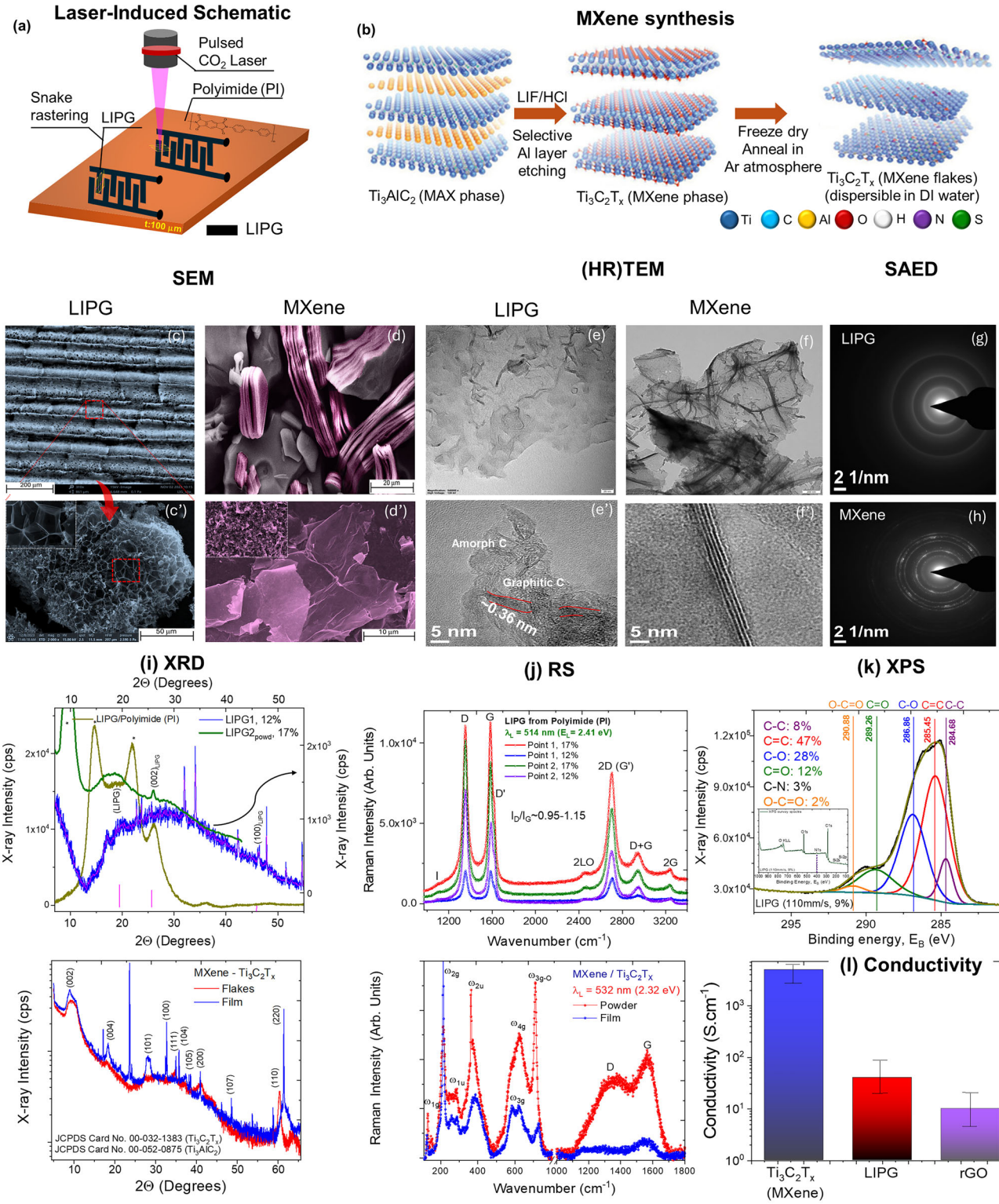

Figure 1. Electrode materials synthesis, morphology, and structural properties. Schematic illustrations of a) laser-induced porous graphene (LIPG) interdigitated electrodes fabrication on polyimide (PI) film (100 micron thick). b) Chemical synthesis of MXene from MAX phase. Representative c,d) scanning electron microscopy; SEM and e,f) high-resolution transmission electron microscopy; (HR)TEM images at two different magnifications revealing surface morphology from (c', d') microscale (e', f') to nanoscale for LIPG and MXene. Scale bars are shown at the bottom of the images. g,h) Selected area electron diffraction (SAED) for LIPG and MXene. i) X-ray diffraction; XRD and j) micro-Raman spectroscopy; RS showing characteristic peaks and bands. k) High-resolution X-ray photoelectron (XPS) spectra showing C—C and C-O chemical bonding. l) Room temperature electrical conductivity (σ_{dc}) of LIPG and painted MXene electrodes compared with thermally reduced rGO_{th}.

show prominent peaks characteristic of sp^2C bonding including the first–order graphitic G peak at ≈1580 cm^{-1} assigned to sp^2 C stretching E_{2g} mode besides disorder–induced dispersive D peak at ≈1350 cm^{-1} correspond to A_{1g} breathing mode or bent sp^2–carbon bonds.[45,69] If PI is carbonized at temperatures ranging from 800 to 1500 °C, the resulting Raman spectra would be like glassy carbon (GC).[70] However, the Raman spectra of LIPG is significantly different from that of GC representative of turbostratic structure. Next is the second-order Raman spectra i.e., 2D peak centered at ≈2700 cm^{-1} originating from zone-boundary K phonons and is due to double-resonant Raman scattering.[71] The other higher-order Raman bands include combination (D+G) and second-order G (2G) bands occurring at ≈2940 and ≈3200 cm^{-1}, respectively. In LIPG, the spectral profile can be fitted with one Lorentzian peak, like single-layer or monolayer graphene, but with a larger full width at half maximum of >50 cm^{-1}. This 2D band profile is typical of those found in 2D graphitic structures with sp^2 C consisting of randomly stacked graphene layers along *c* axis. Finally, D to G band intensity ratio (I_D/I_G) indicates a high degree of crystalline graphene formation in LIPG film. Using Raman spectroscopic data, the sp^2 C crystallite size in *a* axis (L_a) can be calculated from the integrated intensity ratio of G peak (I_G) and D peak (I_D) can be calculated following Equation (3):[72]

$$L_a = \left(2.4 \times 10^{-10}\right) \times \lambda_L^4 \times \frac{I_G}{I_D} \tag{3}$$

where λ_L (= 514 nm) is the excitation wavelength and L_a turned out to be ≈ 6.8–7 nm for as-synthesized LIPG. As for defect number density, n_D (cm^{-2}) and the mean distance between two adjacent defects or inter-defect distance (L_D, nm) are calculated from:

$$L_D^2\left(nm^2\right) = \left(1.8 \pm 0.5\right) \times 10^{-9}\right) \lambda_L^4 \times \left(\frac{I_D}{I_G}\right)^{-1} \tag{4}$$

For excitation laser wavelength 514 nm (2.41 eV), L_D is obtained from:

$$L_D\,(nm) = \sqrt[2]{1.26 \times 10^2 \left(\frac{I_D}{I_G}\right)^{-1}} \tag{5}$$

and the defect density is calculated by $n_D(cm^{-2}) = 10^{14}/(\pi L_D^2)$ such that:

$$n_D\left(cm^{-2}\right) = 2.58 \times 10^{11} \left(\frac{I_D}{I_G}\right) \tag{6}$$

The average values of n_D from Equation (6) is ≈7.0×10^{12} cm^{-2} (≈1.5±0.06 × 10^{10} cm^{-2} for pristine monolayer graphene).[73] For MXene film, five broad peaks with one weak band are observed. The Raman peaks at 200 and 723 cm^{-1} are attributed to the non-stoichiometric titanium carbide (Ti-C) and C—C vibrations (A_{1g} symmetry) of the oxygen-terminated MXene, $Ti_3C_2O_2$.[61] However, in another observation is the absence of Raman band at ≈150 cm^{-1} indicates less or no anatase TiO_2 phase. The reason may be the laser power was low enough to prohibit Ti_3C_2 oxidization. The peak at ≈620 cm^{-1} is from E_g vibrations of the C atoms in the OH-terminated MXene. The peaks at 389 and 589 cm^{-1} are ascribed to O atoms with E_g and A_{1g} vibrations, respectively. The 282 and 519 cm^{-1} (the latter mode is enhanced when 758 nm excitation wavelength was used) are occurring due to the contribution of H atoms in the OH groups of $Ti_3C_2T_x$ and possible low density of anatase (TiO_2) phase on the surface of $Ti_3C_2T_x$.[61] Regarding broad peaks ≈1370 and 1600 cm^{-1}, they belong to the D and G bands of the disordered and amorphous carbon structures with sp^2 C configuration, respectively, particularly for smaller flakes.

As for the surface chemical structure characterized by XPS (X-ray photoelectron spectroscopy), it provides binding energies and changes in the oxidation state of LIPG film, Figure 1k shows XPS spectra of C1s region. Specifically, it shows a primarily sp^2 carbon peak along with oxygen moieties related to hydroxyl (—OH) and carbonyl (C═O) groups with a small portion of carboxyl (—COOH) groups and sp^3C bonding. The hydroxyl groups are incorporated at vacant sites and help to stabilize the defect by bonding to the under-coordinated carbon atoms. Quantitatively, the XPS spectrum shows C═C peak (285.45 eV, 47 at.%) followed by C—C peak (284.68 eV, 8 *at.%)*, with somewhat weaker C—N peak (400.7 eV, 3%), C—O (286.26 eV, 28 at.%), C═O (289.26 eV, 12 at.%) and O—C═O (290.38 eV, 2 at.%) peaks. It suggests that LIPG electrodes are dominated by sp^2 C atoms, agreeing well with the Raman and XRD results. Finally, the presence of defects, C—O and C—N bonds (nitrogen incorporated LIPG from the carbon precursor PI) possess differing and tunable electroactivity depending upon the location and hybridization, chemically showing acid–base properties due to electron–withdrawing effects of *sp*–hybridized oxygen (carbonyl groups) and donating effects of sp^2–hybridized oxygen (hydroxyl and carboxylic groups). The negatively charged pyridinic-N and pyridinic-N-oxide help in electron transfer through the nanocarbons and interfacial interactions[74] The oxygen groups tend to attach defects, and nitrogen atoms contribute to increased surface as they are located at the periphery of graphene sheets. The resulting high electrical conductivity along the trace of laser induction measured with conducting silver paint on two regions of LIPG films and silver alloy wire gives rise to sheet resistance $R_S(= \frac{\pi}{ln2}\frac{\Delta V}{I})$ ranged 40–50 Ω cm^{-2} depending upon the scan speed (110–140 mm s^{-1}) and laser power (9%–17%). Corresponding electrical conductivity σ $(= \frac{1}{R_S \times t})$ at room temperature is 6–8 S cm^{-1}, where *t* is the thickness of LIPG (≈1.5 µm). See Figure 1l, which provides the room temperature electrical conductivity comparison as a histogram for LIPG, thermally reduced rGO, and MXene films of 570 nm (0.57 µm) thick, the latter was much higher than graphene–based films. To note, the electrical conductivity of MXene films depends on the flake size and flake-to-flake contact resistance, and thinner MXene films being semitransparent are useful for flexible and transparent micro-supercapacitors.[61] See also Figure S1 (Supporting Information) shows AFM images of MXene flake and electrode film thickness used for calibration.

2.2. Electrochemical Properties (Cyclic Voltammetry, Electrochemical Impedance Spectroscopy) of Asymmetric Supercapacitors Under Different Electrolyte Compositions

Following structural and morphological characterization, we now focus on the electrochemical properties of fabricated

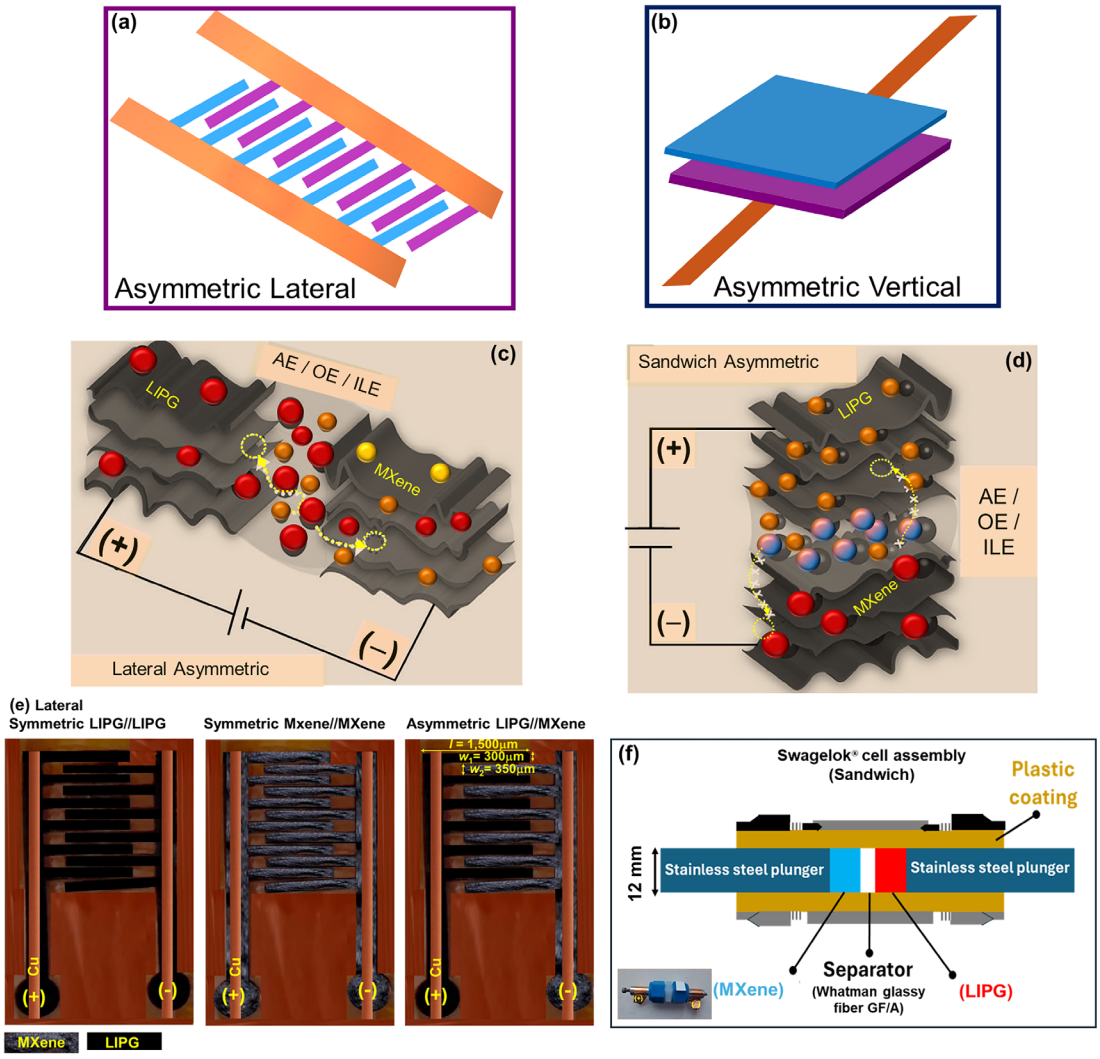

Figure 2. Designing asymmetric electrochemical devices. Schematic illustrations of asymmetric (a) lateral and (b) sandwich micro-supercapacitor devices alongside (c) interdigitated and (d) sandwich device configurations demonstrating ion transportation for positive LIPG and negative MXene electrodes. Shown are (e) top view digital photographs of interdigitated lateral symmetric (LIPG//LIPG, MXene//MXene) and asymmetric (MXene//LIPG) micro supercapacitors with copper tape and (f) Two-electrodes Swagelok sandwich configuration set up. Inset shows digital photograph of Swagelok cell used. Devices schematics shown here are used throughout article figures.

electrode assembly under different electrolytes. **Figure** 2 shows the schematics and digital photographs of all the electrodes and 11-finger lateral asymmetric micro-supercapacitor devices alongwith a two-electrode 'Swagelok' cell assembly for asymmetric sandwich devices. The finger width and length of the electrode patterns are prepared using LightBurn Beta software. We see clearly the well-defined patterns with reasonable homogeneous spacing demonstrate the effectiveness of synthetic strategies. We used optical and electron microscopy to measure the interfinger spacing and finger width yielding finger spacing of 1,500 µm and widths of ≈300 and 400 µm for LIPG and MXene, respectively. Specifically, we examined the electrode kinetics and evaluated the performance of MXene-based asymmetric supercapacitors (MXene//LIPG) in the two-electrode configuration using $Ti_3C_2T_x$–MXene and LIPG as the negative and positive electrodes, respectively, and the results are compared with symmetric (MXene//MXene) supercapacitors in both lateral (coplanar)(Figure 2a,c) and sandwich (cofacial) (Figure 2b,d) configurations along with images of lateral (Figure 2e) and coin cell electrode assembly (Figure 2f). Important to note that the interdigitated lateral device (other than a sandwich) configuration is scalable, flexible, binder, and current–collector free. More than 100 micro-supercapacitors can be produced on a single platform in 30 min. or less for flexible electronics and on-chip uses to be integrated with CMOS or MEMS in a single chip. Therefore, the rapid development of miniaturized devices allows for compact on-chip energy storage solutions. Additionally, MXene is strategically chosen as the negative electrode since it is prone to oxidation under aqueous electrolyte at high positive (anodic) potential in 2-electrode configuration as a positive electrode and may require an overcoat for stability improvement. To avoid the voltage window limitation in MXene, asymmetric electrode design with

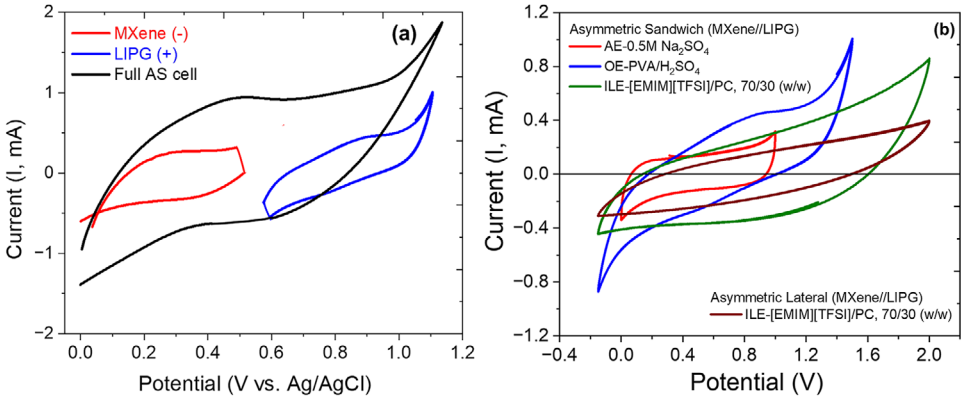

Figure 3. Cyclic voltammograms of individual and asymmetric electrodes. a) CVs of individual electrodes and micro-supercapacitors in a three-electrode configuration recorded at 10 mV s^{-1}. b) Comparison between asymmetric micro-supercapacitors under different electrolytes recorded at scan rate 20 mV s^{-1}.

LIPG as a positive electrode helped to widen the voltage window leading to operation at higher energy densities.

Using a silver wire reference electrode in contact with the electrolyte in single-compartment 3-electrode cell configuration, we distinguished the performance of individual electrodes, as shown in **Figure 3**a. The symmetric cell voltage distribution could be seen with the negative electrode ($Ti_3C_2T_x$) working from 0 to 0.5 V and the positive electrode (LIPG) working from 0.5 to 1.0 V. This CV measurement was done at a low scan rate of 5 mV s^{-1}. This confirms that the total potential window can be increased to 1.0 V by using LIPG as the positive electrode. Having an extended voltage window, the asymmetric interdigitated micro-supercapacitors anticipated improved energy density than the symmetric one at similar power densities. It was also noted that at high scan rates, the symmetric device was marginally better than the asymmetric one due to the higher electrical conductivity of MXene compared to LIPG, which causes all-MXene symmetric devices to have a higher rate capability. Moreover, these asymmetric devices are investigated under three different electrolytes namely, aqueous (AE; Na_2SO_4), organic (OE; polymer gel PVA/H_2SO_4), and aprotic ionic liquid (ILE;[EMIM][TFSI]/PC). Also shown are the cyclic voltammogram (CVs) profiles comparing asymmetric devices under different electrolyte compositions (Figure 3b) show a larger operating window for ILE followed by OE and AE environment besides subtle changes in profiles. To this end, the CVs with varying scan rate are presented in **Figure 4** for AE-sandwich (panel a), OE-sandwich (panel b), ILE-sandwich (panel c), OE-lateral (panel d), ILE-lateral (panel e), symmetric AE-sandwich (panel f), OE-sandwich (panel g), and ILE-sandwich (panel h). Cyclic voltammetry (CV) is performed to examine electrode kinetics in terms of reduction/oxidation (redox) processes, and it is observed that the supercapacitors operate within the voltage window of 0 – 1.0 V, 0– 1.6 V,-0.6– 0.8 V, and 0– 2.0 V for aqueous, organic and ionic liquid electrolytes, respectively. Qualitatively, they show a reasonable rectangular CV shape without any redox peaks, indicative of good capacitive behavior of the two dissimilar yet 2D layered electrode materials. Quantitatively, we determined the areal (C_A) and gravimetric capacitance (C_g) with scan rate following Equations (7) and (8):

$$C_A = \frac{1}{2Av}\left(\frac{1}{(V_f - V_i)}\right)\int_{V_i}^{V_f} I(V)\,dV \tag{7}$$

$$and\ C_g = \frac{1}{2mv}\left(\frac{1}{(V_f - V_i)}\right)\int_{V_i}^{V_f} I(V)\,dV \tag{8}$$

where A the total geometric surface area of active electrodes (in cm^2), and m the mass of active electrodes in mg, v the voltage sweep rate (in $V{\cdot}s^{-1}$), V_f and V_i the potential limits of CV curves, $I(V)$ the voltametric current (in amperes), and $\int_{V_i}^{V_f} I(V)dV$ the integrated area from CV curves. The calculated specific capacitance values are plotted as in Figure 4 (panels i–l) for all the asymmetric and symmetric devices in both configurations. As an example, at 5 or 10 mV s^{-1}, the areal (C_A)[and gravimetric capacitance, C_g] were calculated to be ≈11.2 mF cm^{-2} (400 F g^{-1}), 2.6 mF cm^{-2} (120 F g^{-1}), 5.1 mF cm^{-2} (290 F g^{-1}), 6.2 mF cm^{-2} (320 F g^{-1}), and 5.4 mF cm^{-2} (260 F g^{-1}), for asymmetric AE-sandwich, OE-sandwich, OE-lateral, ILE-sandwich, and ILE-lateral devices, respectively, in contrast to 8.9 mF cm^{-2} (300 F g^{-1}), 2.2 mF cm^{-2} (100 F g^{-1}), 4.2 mF cm^{-2} (190 F g^{-1}), and 4.4 mF cm^{-2} (200 F g^{-1}) for symmetric devices. Corresponding estimated volumetric capacitance values are 149, 35, 68, and 83 F cm^{-3}. The areal capacitance for OE-sandwich and OE-lateral devices is higher than those reported of a voltage window of 1.6 V despite using a thicker MXene electrode (≈2.4 mF cm^{-2} and 80 F cm^{-3} at 1V for 0.3 µm thickness prepared with spray coating).[75,76] Interestingly, we also determined the C_A value for symmetric LIPG that turned out to be 1.2 mF cm^{-2} which is 2.5 times higher than exfoliated graphene (0.462 mF cm^{-2}) and rGO (0.41 mF cm^{-2}),[77] and the enhancement originated from inclusion of topological defects, functional groups and dopants,[78] accounted for higher values for asymmetric supercapacitive

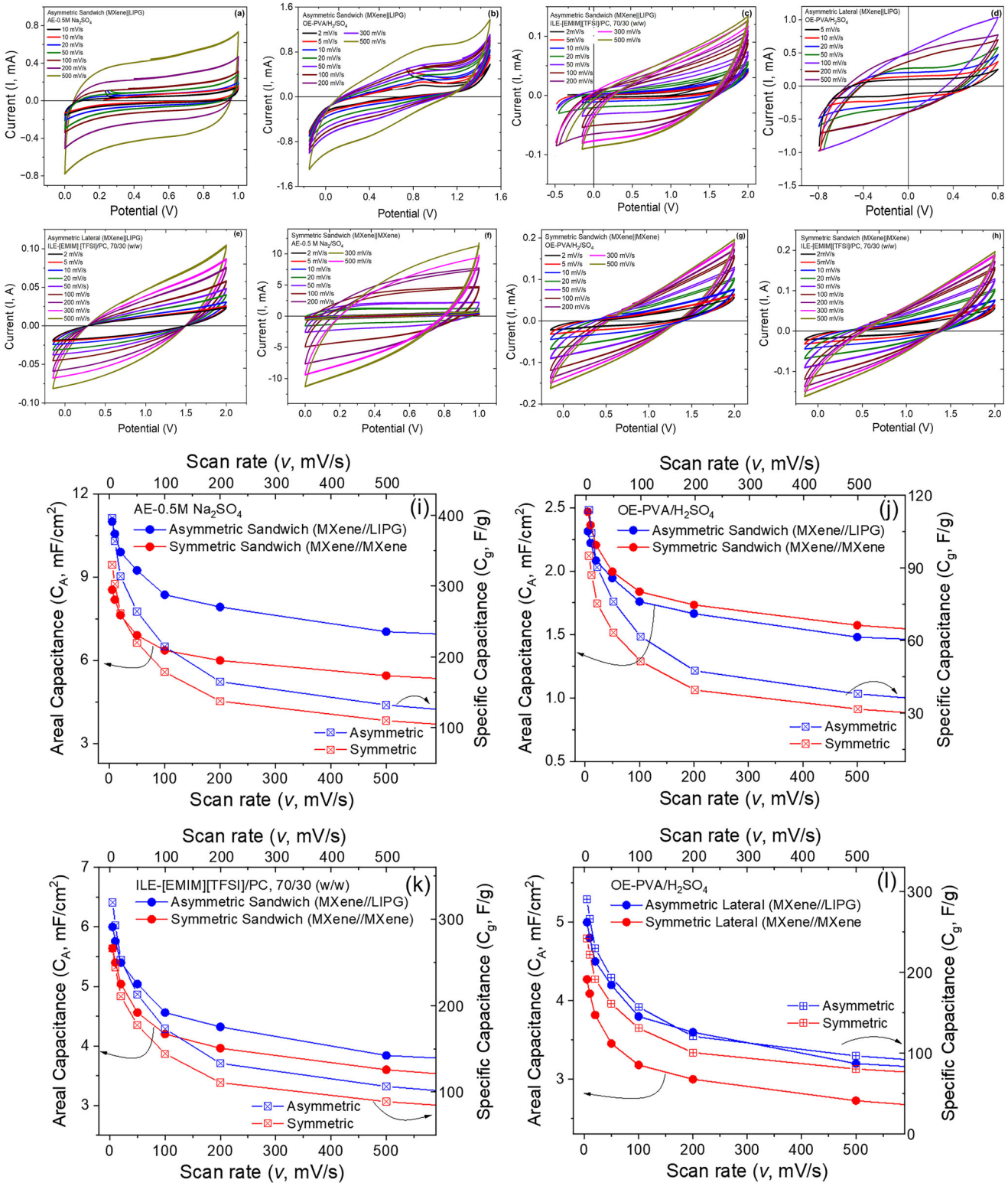

Figure 4. Electrochemical charge-potential profiles. Potentiostatic cyclic voltammograms (CVs) at different scan rates (5–500 mV s^{-1}) in two-electrode setup for asymmetric micro supercapacitor in a) aqueous electrolyte (AE) b) organic electrolyte (OE) c) ionic liquid electrolyte (ILE) and in lateral configuration in d) organic electrolyte (OE), and e) ionic liquid electrolyte (ILE). CVs of symmetric micro supercapacitor in sandwich configuration in f) AE g) OE and h) ILE. Corresponding areal (C_A) and gravimetric specific capacitance (C_g) variation in i) AE j, k) OE and l) ILE for both asymmetric and symmetric micro supercapacitors.

devices studied here. The interdigitated architecture allows facile in-plane diffusion of ions between electrodes while sandwich architecture impedes ion transport pathways between the layers of electrode materials for OE environment. On the other hand, the capacitance (or charge storage) values for AE and ILE are higher for sandwich configurations followed by OE as anticipated since the ion transportation is obstructed. Charge transfer reactions include pseudo-capacitance processes such as specific adsorption are captured by electrochemical impedance spectroscopy (EIS) through deviations from the ideal capacitive response in both Nyquist (−Z″ *versus* Z′) and Bode (|Z| versus frequency) plots. The asymmetric supercapacitors impedance spectra in terms of Nyquist (**Figure 5**, panels, a,d,g,j), Bode–Bode (Figure 5, panels b,e,h,k), and phase response with semi log frequency (Figure 5, panels c,f,i,l) for AE-sandwich, OE-sandwich, OE-lateral, and ILE-sandwich devices along with symmetric configuration and simulated fits are provided. Qualitatively, they exhibit good supercapacitive behavior with a small or depressed semicircle arc (i.e., solid-electrolyte interphase and grain boundary) in the high-frequency region and a straight 45° sloping line (i.e., solid-state diffusion in bulk electrolyte and ions diffusion into pores of electrode) in the mid to low-frequency range attributed to Warburg impedance (Z_W), related to charge transfer process at the electrode-electrolyte interface and semi-infinite mass diffusion, respectively.[79,80] The trend in increasing slope exhibits a capacitive nature related to the film charging mechanism which is typical characteristic for mesoporous electrodes with 3D network. The phase change of almost 70°–80° indicates good capacitive behavior of the asymmetric supercapacitors. Moreover, the impedance spectra were fitted with R-CPE (Constant Phase Element) circuit, and the quantitative values of various parameters were extracted following EEQC simulation in the EC-Lab software consisting of R_s(CPE(R_{ct}W)) elements (Figure 5m) with fitting error $\chi^2 \approx 10^{-4}$. Typically, a numerical simulation of the RC Circuit within the EC-lab software is performed using the Runge–Kutta 4 order (RK4) method, which is compared with the exact impedance equation for RC circuit employed. In the proposed circuit simulation, R_S refers to the equivalent series resistance made up of solution resistance caused by ions in the electrolyte that remains the same for all the devices in a particular electrolyte, resistance inherent in the active electrode material, and interfacial resistance between the electrode and current collector, CPE represents a non-ideal behavior of electric double layer capacitance arising due to spatial heterogeneities in hierarchical porous and layered electrode surfaces at the electrified interface and impedance displaying a frequency-independent phase angle different from 90° as depicted here. Frequency dispersion is a commonly acknowledged behavior in the impedance response of electrode/electrolyte interfaces, which reflects distribution in time constants of interfacial processes, has been reported to originate from surface heterogeneity of structural properties, specific anion adsorption, coupling between Faradaic and double layer charging currents, geometry-induced current and potential distributions.[71] To model this behavior, a fractional element, CPE, in impedance form is expressed as follows:

$$Z_{CPE} = \frac{1}{Y_{CPE}} = \frac{1}{Q(j\omega)^{\alpha}} = \frac{1}{Q}[(\omega)^{-\alpha} \exp(-j\alpha/2)] \quad (9)$$

where Q is the pre-exponential factor related to admittance Y and = 1/|Z| at $\omega = 1$ rad/s where ω is the angular frequency, and α is the vital CPE exponent. When $\alpha = 1$ (ideal capacitor), Q has units of capacitance, i.e., μF cm^{-2} (or mF cm^{-2}), and represents the interfacial capacity. When α <1, the system shows behavior attributed to surface heterogeneity or to continuously distributed time constants for charge-transfer reactions and $\alpha = 0$ for pure resistance. CPE parameters Q along with exponent α are independent of frequency and a prerequisite for calculation of characteristic capacitance defined by Brug et. al.[81] From the EEQC fitting results, the CPE exponent α ranged between 0.75 and 0.81 for all the devices investigated indicate a decrease in frequency dispersion of capacitance, increasing spatial homogeneity, and closer to an ideally polarizable interface. Next is R_{ct}, the charge transfer resistance associated with the electron transport resistance from solvated ions in electrolyte crossing the electrode/electrolyte interface and passing through the electrodes, which activates polarization. The smaller the semicircle, the smaller the R_{ct}, indicative of more electron-transfer pathways and faster electrolyte-ion diffusion, which can lead to enhanced cycling stability and rate performance. In other words, R_{ct} is inversely proportional to the current density, suggesting an excellent inner electrical network built by the electrodes. Typically, a higher R_{ct} value suggests sluggish charge transfer. Finally, W is the Warburg impedance (Z_W) in low frequency region related to R_{ct}, diffusion coefficient D_0, and heterogeneous electron transfer rate, k_{ET} by: $Z_W = R_{ct}\lambda/(\omega)^{1/2}$ where $\lambda \approx k_{ET}/2\sqrt{D_0}$, given electrochemical reactions are interfacial, and mass transport arises due to diffusion processes. The total interfacial capacitance can also be extracted from EIS data by adopting a graphical approach developed by Tribollet *et. al.*, for systems exhibiting frequency dispersion effects.[82] Effective capacitance C_{eff} is calculated at each applied frequency using the following:

$$C_{eff} = \sin\left(\frac{\alpha\pi}{2}\right)\frac{-1}{Z_{im}(2\pi f)^{\alpha}} \quad (10)$$

where Z_{im} the imaginary part of impedance and f is the applied frequency in Hz. The final capacitance values were obtained by averaging the determined C_{eff} values within the frequency range where the phase angle of the system was ≥ 75–80° per absolute value (corresponds to a non-ideal polarizable interface). The elements used for fitting the EIS data and C_{eff} values are provided in **Table 1**. As for Bode magnitude plots, they represent the ratio of alternating voltage to alternating current (i.e., impedance) amplitude versus frequency, irrespective of their phase shift, which decreases with increasing frequency with occasional broad peaking behavior. This suggests that the devices can be electrically simulated to an assembly of parallel RC components normal to the electrode surface. Such electrodes exhibit charge-trapping capabilities, and they are promising supercapacitors. Considering the entire system for evaluating frequency-dependent capacitive behavior, it is known that the low frequency of the real part (C′) corresponds to the effective capacitance of supercapacitor devices, and the imaginary part of capacitance (C″) is related to energy dissipation due to quasi-reversible process. Thus, the electrode response time can be estimated from the frequency that correspondeds to the maximum of Bode–Bode plots. The response time constant measured

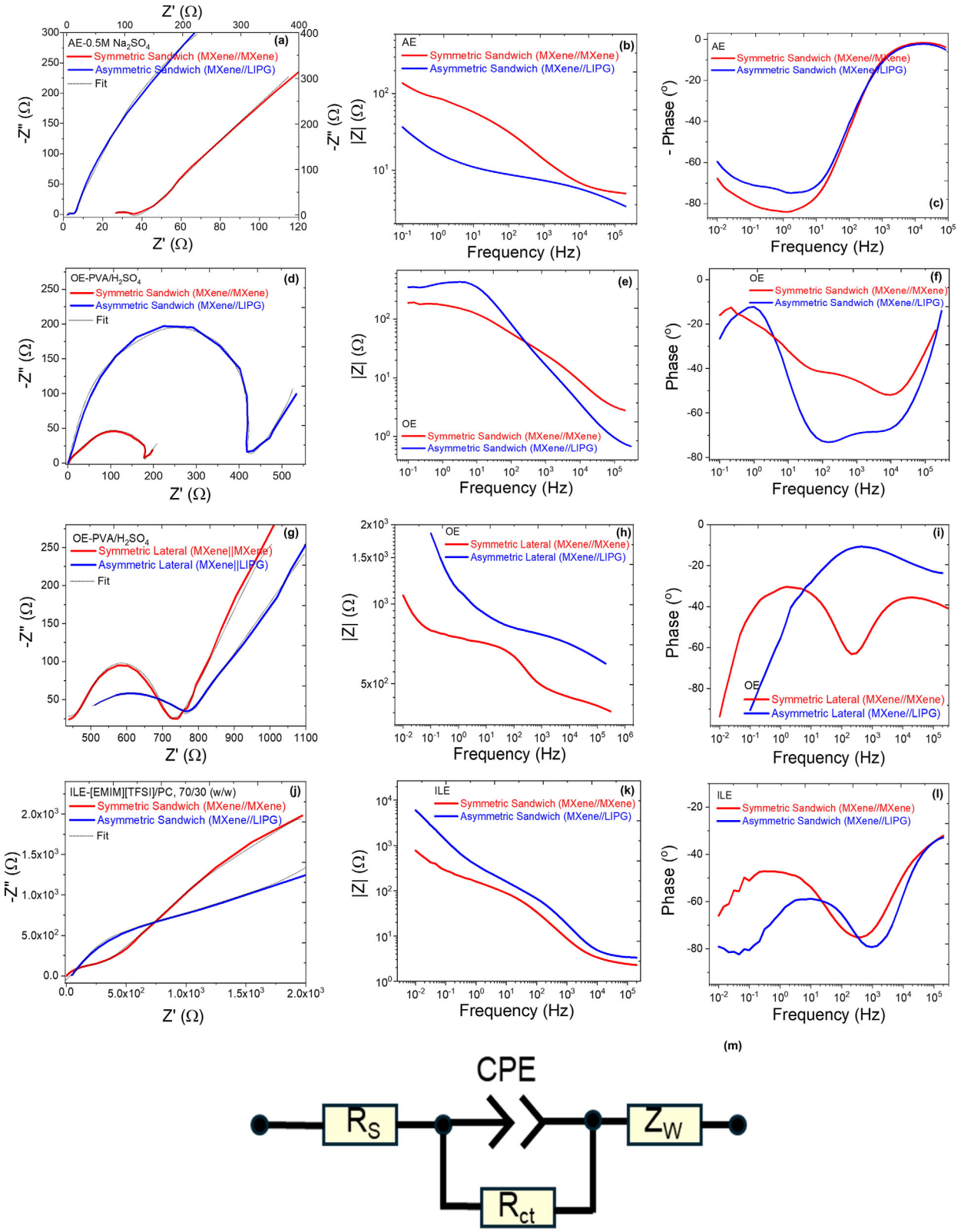

Figure 5. Electrochemical impedance spectroscopy. Representative a,d,g,j) Nyquist plots showing -Z″ (imaginary) versus Z′ (real) behavior alongwith circuit simulation fits (dotted line). b,e,h,k) Bode–Bode plot showing impedance magnitude with frequency. c,f,i,l) phase behavior, all for asymmetric and symmetric devices in sandwich and lateral configurations under AE, OE, and ILE environments. m) Shows CPE equivalent circuit used to fit the impedance spectra extracting various electrode parameters.

Table 1. Summary of electrochemical impedance spectroscopy parameters simulated with CPE circuit modeling and graphical method for asymmetric and symmetric devices in aqueous, organic, and ionic liquid electrolytes.

Electrode Configuration and Electrolyte Type	R_s (Ω)	Q	R_{ct} (Ω)	α	Z_W (Ω)	C_{eff} (mF/cm^2) $_{@1Hz}$	Fitting Error (%)
AE-0.5M Na_2SO_4 /H_2O							
Asymmetric Sandwich	2.021	11.05	1.03×10^1	0.791	2.73	10.48	5.235
Symmetric Sandwich	4.206	8.75	1.18×10^1	0.789	1.92	8.42	4.724
OE-PVA/H_2SO_4							
Asymmetric Sandwich	26.032	2.35	4.37×10^2	0.785	4.45	2.26	3.582
Symmetric Sandwich	15.912	2.55	3.19×10^2	0.758	3.63	2.47	4.943
Asymmetric Lateral	27.231	5.15	1.68×10^2	0.779	3.87	6.01	5.891
Symmetric Lateral	16.432	4.25	2.28×10^2	0.810	3.68	5.13	6.319
ILE-[EMIM][TFSI]/PC							
Asymmetric Sandwich	6.12	6.15	6.28×10^1	0.803	1.88	6.42	6.115
Symmetric Sandwich	5.831	5.87	7.19×10^1	0.773	1.32	5.29	5.141
Asymmetric Lateral	4.320	4.51	5.28×10^1	0.768	2.45	3.88	7.032
Symmetric Lateral	5.354	4.12	6.29×10^1	0.813	2.45	4.31	4.671

R_s is the uncompensated electrolyte resistance. α is the constant phase element exponent associated with extent of electrochemical double-layer capacitance at the electrode-electrolyte interface. R_{ct} is the charge transfer resistance between the interface of electrode and electrolyte. Q is the constant phase element exponent associated with electrochemical double-layer capacitance at the electrode–electrolyte interface. Z_W is the Warburg impedance associated with impedance in the low frequency region. C_{eff} is the total interfacial capacitance determined from graphical method. The error mentioned represents a relative standard error.

for AE-sandwich (τ_{RC} = 12.3 ms) is comparable to ILE-sandwich (τ_{RC} = 14.1 ms), as compared with OE-sandwich (τ_{RC} = 5.8 ms) and OE-lateral (τ_{RC} = 1.7 ms) devices. These values arise due to a larger RC constant, contact resistance between electrode active material, and it is due to a significant increase in specific capacitance. Summarizing the traditional electrochemical measurements, it is reasonable to claim the dual functionality endowed by a porous or extended network of graphene nanosheets in LIPG possessing higher surface area and layered MXene–based electrodes having good electronic conductivity properties enables faster charge transfer kinetics through the electrode/electrolyte interface. These findings motivate us to evaluate the heterogeneous electron transfer rate (k_{ET}) qualitatively for all the electrodes/devices under various electrochemical environments following impedance spectroscopy. For instance, the apparent electron transfer rate constant (k_{app}) can be obtained from Equation (11):[73]

$$k_{app} = RT/n^2\ F^2 A R_{ct} c_0 \tag{11}$$

where A is the experimentally determined area of the active electrode, n (= 1) is the number of electrons transferred, F is the Faraday constant, R the gas constant, T the temperature, c_o the concentration of electrolyte species, and R_{ct} value is extracted by fitting Nyquist plots at medium frequencies. At first, the charge transfer process consists of multiple steps, wherein the solvation/desolvation process has been recognized as the rate-determining step. Therefore, it is necessary to reduce activation energy ($R_{ct} = Ae^{-Ea/RT}$) of solvation and desolvation to improve the reaction kinetics at the interface.[83] Secondly, the kinetics of charge transfer are also reflected in charge transfer resistance (R_{ct}) such that a higher value suggests delayed reaction kinetics or vice versa. A higher R_{ct} value for OE suggests slower electron transfer kinetics as compared to AE and ILE yielding to faster electron transfer kinetics. The incorporation of surface defects, functional groups, and nitrogen doping atoms into the component electrodes i.e., MXene and LIPG determined through Raman spectroscopy and XPS analysis, plays a vital role in describing the observed charge transfer kinetics. Moreover, the formation of sp^2 hybridized carbon phases, enriched with edge dislocation sites, and hydrogen bonding groups represent significant factors that contributed to the improved electrochemical rate performance. Thus, the defects and specific functional groups lead to effective electrode kinetics and higher value of electron transfer rate constant. Furthermore, the high electrochemically active surface areas of MXene and LIPG makes the electrodes in asymmetric devices persistently attractive.

2.3. Electrochemical Performance (Cyclability, Capacitance Retention, Coulombic Efficiency, Ragone Plot) of Asymmetric Supercapacitors Under Different Electrolyte Compositions

Galvanostatic charge–discharge (GCD) profiles measured with varying current density (0.08–0.84–1.0 A g^{-1}) to study the rate capability (cyclability), capacitance retention, Coulombic efficiency, and subsequently derive specific energy and power densities of the asymmetric MSCs, are shown in **Figure 6**a–i. Also shown is the comparison of the GCD profile for asymmetric sandwich devices under different electrolytes (Figure 6) at a particular current density exhibiting subtle differences in their shape, thus affecting their corresponding performance. The GCD profiles show apparent sloping yet asymmetric nonlinear curves, indicating faster redox reactions of the electrode and capacitor-like responses combined with a surface redox reaction. The kinetics of the redox reaction during the discharge and charge processes identifies MXene as a promising negative electrode for asymmetric supercapacitors. Moreover, the macroscale morphology of 3D interconnected porous framework with nanopores on graphene sheets

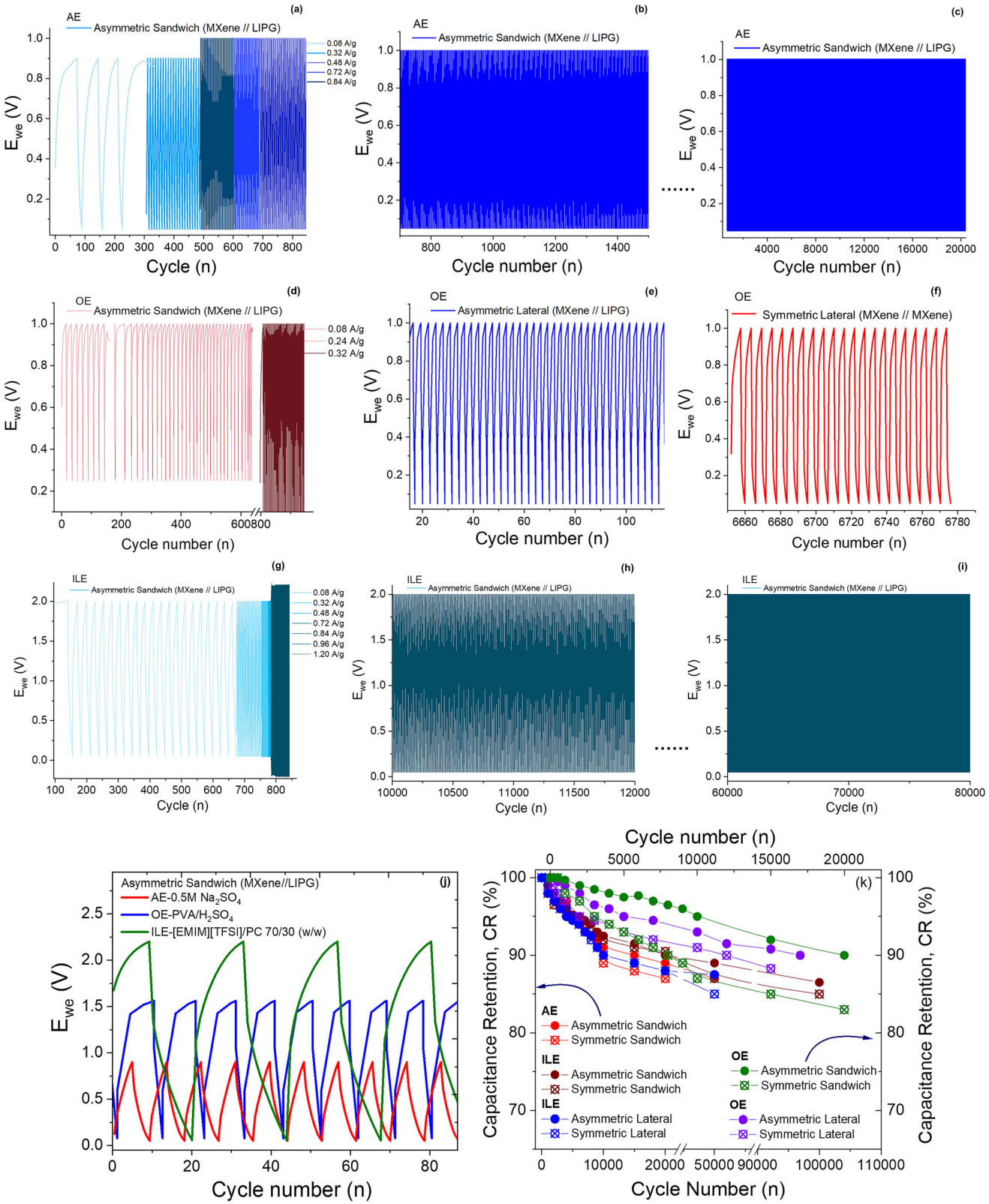

Figure 6. Galvanostatic charge-discharge (GCD) and cyclability profiles. Representative GCD profiles between 0.08 and 0.84 A/g current density for a–c) AE-asymmetric sandwich d) OE-asymmetric sandwich e) OE-asymmetric lateral f) OE-symmetric lateral g–i) ILE-asymmetric sandwich showing characteristic discharging capacitor shapes. j) Comparison of asymmetric micro-supercapacitors under different electrolytes at current density 0.16 A g^{-1}. k) Summary of capacitance retention percentage for all devices and in all configurations.

(LIPG) results in decreased diffusion distance of electrolyte ions. On a closer look, the supercapacitor with OE-sandwich configuration illustrated the lowest GCD discharge time (Figure 6e). The discharge period declined with increasing current density, which implies the charge storage ability is affected by the fast diffusion of ions especially for AE and ILE. Moreover, the AE and ILE amplified the GCD time, which exhibits an improvement in the charge storage of the asymmetric sandwich and OE-lateral MSCs. Quantitatively, the GCD profiles also designate the charge storage performance depending upon the ion transport and accumulation within the electrochemical double layer of the electrodes. Alternatively, the discharge time is related to the capacitance and storage capacity with discharge parameters following:

$$C_g = \frac{2I \times \Delta t}{m \times \Delta V} \tag{12}$$

where I the discharge current, Δt is the discharge time (t_d) determined, and ΔV the voltage difference (*i*R drop) in the discharge of working electrodes. For instance, the optimal C_g values of asymmetric supercapacitor electrodes including varied combinations of electrolytes (AE, OE, and ILE) were computed to 130.2 and 127.6 F g^{-1} after 100th and 1000th cycles, respectively. Noticeably, there is a decrease of 5% in C_g values after 5000 GCD cycles compared to its initial performance. The utmost C_g value calculated at low current densities (0.08 or 0.1 A g^{-1}) is due to the substantial transfer of ionic species through all layers of constitutive porous electrodes, and they are comparable to those determined using CV profiles provided above and higher than those previously reported ASCs.[84–86]

The cyclic GCD tests were performed to evaluate long-term performance (see Figure 6k) by comparing with varied cycle numbers ranging 500, 1000, 5000, up to >200 000 cycles for the fabricated asymmetrical supercapacitors with various electrolytes. In these tests, the devices were charged to the highest potential of the respective electrolyte (1.0, 2.0, 2.5 V) and then discharged to 0.01 V (0r 0.05 V) at a fixed current density of 0.84 or 0.96 A g^{-} yielding comparable results. Figure 6k depicts the stability as capacitance retention (CR) percentage derived from specific capacity with cycle number from its initial value for all asymmetric (and symmetric) supercapacitor devices under different electrolytes. The results show that the AE- and ILE-sandwich supercapacitor devices depict more stability in comparison to OE-sandwich supercapacitors suggestive of faster capacitance lossdue to rapid decline in ions mobility. Additionally, it was noticed that supercapacitors revealed marginal performance losses at initial cycling due to arriving at the maximum ion transfer capability of electrolyte, but it increased after a few cycles in compliance with the observation noted and reported by others. The CR remained at >80% when the areal mass loading was 0.6 mg cm^{-2} demonstrating immense potential for high mass loading (at least 10 times) in practical applications while ensuring improved performance and mechanical robustness. Due to the highly interconnected porous network and developed electron conductive pathways of novel MXene-based ASC combining MXene//LIPG electrodes under three different electrolytes accounts for their superior (≈80–85%) rate performance compared with the previously reported ASC supercapacitors (≈65–70%) using different electrode materials and electrolytes after 5000 cycles.[84,85] Moreover, the prolonged cycling (up to ≈100 000) confirms that the electrodes in both the asymmetric (and symmetric) lateral and sandwich architectures appear physically intact and maintain their morphology (*via* SEM) and structure (*via* Raman spectroscopy) without any chemical or physical degradation (see Figure S2, Supporting Information showing SEM images and Raman spectra of pre-and post-cycling of MXene electrodes) except occasional swelling of MXene layers due to electrolyte ions intercalation thereby prohibiting restacking of MXene flakes and lack of TiO_2 formation. The decomposition of electrolytes may be responsible for the observed CR values after a prolonged time.

The GCD profiles can also provide device parameters such as Coulombic efficiency and energy efficiency, η_E and they must be evaluated to compare with the reported values in the literature, together with the Ragone plot, described in subsequent section. Coulombic efficiency (abbreviated CE) is mathematically defined as: $CE = Q_{output}/Q_{input} = Q_{dis}/Q_{ch} = I_{dis}\ t_d\ /\ I_{ch}\ t_c$, where Q is the amount of charge delivered from the electrode during discharging (Q_{dis}) to the charge stored on the electrode during charging (Q_{ch}), also related to the rapid reaction rate, I and t represent current and time, respectively. For "constant current" GCD operation, $I_{dis} = I_{ch}$ and thus, $CE = t_d\ /\ t_c$ or percentage ratio = CE × 100. In general, the ASCs of sandwich device configuration depict CE of 100% since $t_d \approx t_c$. The ASCs have a capacitance retention of ≈85% at 10 000th cycle in a wide voltage of 2.5V, with CE near to 100%. Such a wide voltage can cause capacity decay resulting from the degradation of oxygen functionalities on MXene electrode surface, especially for OE-sandwich devices. Nevertheless, for an asymmetric supercapacitor with 100% CE does not necessarily imply the reversibility of electrochemical reaction, meaning energy density in charge (E_c) and discharge (E_d) regions are not equal ($E_d \neq E_c$). Energy efficiency η_E defined by $\frac{E_d}{E_c}$ and the quantity 1-η_E (or $\eta_E < 1$) represents energy losses due to irreversible parasitic reactions occurring due to impurities and electrolyte/electrode decomposition, which means shorter lifespan, higher self-discharge and iR (Ohmic) loss related to overall voltage profile linked to the electrode chemistry and device configuration. For practical applications, the device should have low resistive component electrodes where impedance spectroscopy is useful for direct evaluation of dissipative properties and should be fabricated by increasing loading amount (mass or thickness) while assembling soft-package flexible asymmetric cells. The specific energy density, ED, refers to the stored electrochemical energy per unit mass (gravimetric, ED_g) and volume (volumetric, ED_V denoted) of the electrode defined by:

$$ED_g = \frac{1}{2}\frac{C_g.V^2}{m}.\frac{1}{3600\ s}\left(\text{Wh g}^{-1}\right) \text{ and } ED_V = \frac{1}{2}\frac{C_V.V^2}{\text{V}}.\frac{1}{3600\ s}\left(\text{Wh cm}^{-3}\right) \tag{13}$$

And corresponding volumetric (and gravimetric) power density, PD, are given by:

$$PD_g = \frac{ED_g}{t_d}\left(\text{W g}^{-1}\right) \text{ and } PD_V = \frac{ED_V}{t_d}\left(\text{W cm}^{-3}\right) \tag{14}$$

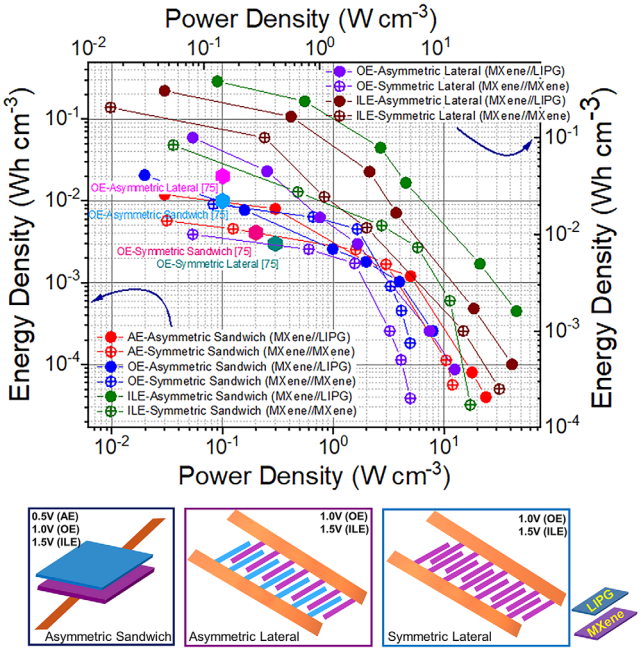

Figure 7. Ragone plot. Variation of volumetric specific energy versus specific power density on log-log scale for asymmetric (MXene/LIPG) and symmetric (MXene/MXene) devices in both the (lateral and sandwich) configurations for various electrolyte compositions along with device illustration. The values for OE-asymmetric devices from[72] are shown for comparison.

where m is the mass of the electrode, V is the volume, 3600 s is 1h and t_d the discharge time. The calculated volumetric specific power and energy densities of the asymmetric (and symmetric) supercapacitors are illustrated in **Figure 7** as a Ragone plot, showing interesting trends depending upon the electrolytes alongwith illustrations of asymmetric sandwich and lateral and symmetric lateral devices with the operating voltage values for the respective electrolytes. It is noted that the specific capacity was calculated according to the mass and volume of active electrode material. The combination of gravimetric and volumetric energy and power densities are summarized in **Table 2**, which are superior to other devices reported in the literature.[84,85] In line with CV results, the asymmetric supercapacitors exhibited much higher capacity than the symmetric device for all device architectures and electrolytes. When we evaluated symmetric interdigitated MSC based on MXene, the maximum voltage window was 0.6 V and it was extended up to 1.0 or 1.1 V by using LIPG as the positive electrode yielding better energy density values for asymmetric devices than those of symmetric at similar power densities for AE and OE environment except for ILE since the operating voltage window was higher (≈2.5 V). Figures 6a,d,g show negligible initial voltage loss (*iR* drop) of the discharge profiles, suggesting lower internal resistance and faster current–voltage response. Specifically, it is shown that among all ASCs, the ILE-sandwich device retained the maximum specific energy of 289 Wh cm^{-3} (or 56 Wh kg^{-1}) at specific power of 0.2 W cm^{-3} (458 W kg^{-1}) followed by asymmetric lateral device under ILE[135 Wh cm^{-3} (or 38.7 Wh kg^{-1}) at specific power of 0.4 W cm^{-3} (334 W kg^{-1})], OE[45 Wh cm^{-3} (or 11.6 Wh kg^{-1}) at specific power of 0.3 W cm^{-3} (74 W kg^{-1})] and AE-sandwich[10.5 Wh cm^{-3} (or 85.2 Wh kg^{-1}) at specific power of 0.2 W cm^{-3} (506 W kg^{-1})] devices, respectively. The energy storage capability is improved via the insertion of extra charge carriers (EMIM and PVA) in the bulk of electrode (interlayer intercalation), macroscale porosity, electroactive sites for redox reaction of ketone (C=O) or carbonyl (—COOH) groups with electrolyte ions on LIPG where ions are adsorbed and interact with pyridinic N heteroatoms. Moreover, asymmetric MXene//LIPG supercapacitors show exceptional rate performance with higher capacity at higher current density, demonstrating excellent rate capability. The faster kinetics for the redox reaction during the discharge and charge processes identify MXene as a promising electrode for asymmetric supercapacitors. At higher specific power, the specific energy of supercapacitors showed a decreasing trend for all electrolytes. However, it is evident that higher energy could still be harvested with the supercapacitor at elevated power densities (0.4 W kg^{-1}). The electrochemical performance demonstrated that this asymmetric system that integrates pseudocapacitive- and supercapacitor-like components is promising to overcome the challenges of capacitance mismatch and sluggish kinetics, bridging the gap between conventional batteries and electrolytic capacitors.

2.4. Design Considerations for Enhanced Cell Voltage of Asymmetric Supercapacitors and Electrode Charging Mechanisms

It is conceivable that the objective comparison of different energy storage systems is not a straightforward task. A series of recommendations are made for electrochemical power sources in which pseudocapacitive electrode (MXene) was coupled with a non-Faradaic, supercapacitive electrode (LIPG), resulting in asymmetric (MXene//LIPG) construction, indicative of the dual functionality.[11] This section delves into indepth discussion of design considerations leading to the observed enhanced cell voltage and high specific energy trends for MXene-based ASCs operating in three different electrochemical environments. Since the energy storage of the asymmetric supercapacitors studied herein is controlled by ECDL electrodes, understanding the electrode charging mechanism is also significant. One of the straightforward approaches to increase the amount of storable energy is by the strategic choice of electrolyte (aqueous versus organic and ionic liquid) which extends the working potential window such as between its lowest unoccupied molecular orbital (LUMO) and highest occupied molecular orbital (HOMO), where the former improves the energy density by increasing the latter parameter value.[13] Also, this is effective since the energy density is proportional to the square value of operating potential (see Equation 13). Moreover, the electrochemical performance with organic (and ionic) electrolytes for pseudocapacitors attaining high energy density is analogous to rechargeable Li-ion batteries.[86] Thus, the charging characteristics of such electrodes in asymmetric devices are found to be vastly different to optimize overall performance which is exemplified by the synergistic hybridization of the pseudocapacitive and supercapacitive electrode components in one device under proper electrochemical environment and experimental conditions, which clearly is a complex matter. **Figure 8** summarizes a hybridization scheme and corresponding

Table 2. Summary of electrochemical performance for asymmetric and symmetric devices in various configurations under aqueous, organic, and ionic liquid electrolytes.

Electrode Configuration and Electrolyte Type	Working potential range (ΔV)	Energy density (mWh cm^{-3}) [Wh kg^{-1}]	Power density (W cm^{-3}) [W kg^{-1}]	Refs.
AE-0.5M Na_2SO_4/H_2O				
Asymmetric Sandwich	1.0	10.5[85.2]	0.2[506]	This work
Symmetric Sandwich	0.8	4.6[23.2]	0.1[210]	This work
OE–PVA/H_2SO_4				
Asymmetric Sandwich	2.0	6.3[37.5]	0.1[62]	This work
Symmetric Sandwich	1.6	10[19.1]	0.1[23]	This work
Asymmetric Lateral	2.0	45[11.6]	0.3[74]	This work
Symmetric Lateral	1.8	10[35.3]	0.1[25]	This work
OE–PVA/H_2SO_4				
Asymmetric Sandwich[a)]	1.0	10	0.1	[75]
Symmetric Sandwich	0.6	4.1	0.2	[76]
Asymmetric Lateral[a)]	1.0	20	0.1	[75]
Symmetric Lateral	0.6	3.0	0.3	[75]
ILE–[EMIM][TFSI]/PC				
Asymmetric Sandwich	2.5	289[56.1]	0.2[458]	This work
Symmetric Sandwich	2.0	34[29.5]	0.4[157]	This work
Asymmetric Lateral	2.5	135[38.7]	0.4[334]	This work
Symmetric Lateral	2.0	90[23.9]	0.3[79]	This work

Note: AE–Aqueous Electrolyte; OE–Organic Electrolyte (Polymer Gel); ILE–Ionic Liquid Electrolyte. PC-Polypropylene Carbonate; Asymmetric–MXene//LIPG; Symmetric–MXene//MXene; LIPG//LIPG; [a)] Asymmetric–MXene//rGO.

charge-potential profiles representing electrostatic and redox behaviors at the electrode/electrolyte interface.[9,87]

In general, for EC applications, during charging ions are moving under the influence of forces resulting from a gradient of chemical potential and electrical field produced by the motion of oppositely charged ions. Hence, the effects of ion/ion and ion/solvent interactions play crucial roles in the charge transfer and mobility of the electrochemical energy systems. In addition, the higher surface area electrodes allow access to aqueous (hydrated), organic, and ionic electrolytes insertion, and good conductivity, which is beneficial in hybridized configuration. Upon polarization, the negative electrode experiences a reversible redox reaction of electrolyte ions in MXene layers, while LIPG positive electrode reversibly adsorbs and releases anions from the functional carboxyl groups and via enolization with carbonyl groups associated with π bonding as an example. Besides ECDL charging, additional redox reactions at the negative electrode in aqueous electrolyte takes place via T_x terminated MXene layers. Also, the negative polarization of the electrode allows permselective (only cations) adsorption/desorption. The charging mechanism at the positive polarization is ion exchange where OH^-, SO_4^{2-}, and$[TFSI]^-$anions accumulate within the open structure of LIPG, resulting in local pH shift and thus, changes in cell potential. Additionally, a larger GCD profile slope than theory proves the adsorption of additional molecules at negative polarity, proportional to electrode charge. The effect of ionic liquid electrolyte is worth discussing since it extends operating voltage and subsequent specific energy density the most in addition to interfacial structural profiles for MXene (and LIPG)/ionic liquid double layer is not fundamentally understood, which is considerably different for ILE from than those from conventional aqueous and nonaqueous organic electrolytes. For instance, the cations (Na^+, PVA, and EMIM/TFSI) and anions (SO_4^{2-}, TFSI) differ in hydration/solvation strength, hence influencing the interface properties. Moreover, the co-existence of solvent molecules and ions inside the electric double layer influences structural characteristics affecting their metrics. With these considerations, we expatiate the energy storage mechanism that is during charging and discharging, anions and cations move toward or depart from the electrodes, and accumulation/separation or rapid charge transfer happens at the capacitive electrodes. For neat EMIM-TFSI at moderate potential, the electronic properties of the electrode govern the overall interfacial capacitance with the least contribution from the electrolyte. The presence of organic solvents significantly changes the composition of the inner layer.[88] In mixtures of EMIM-TFSI with PC solvent as in this work, the complex interplay between electrolyte ions and solvent molecules influences the charge stored at the interface since it depends on the solvent permittivity (ε_r = 64 for[EMIM][TFSI]) and intermolecular forces between the electrolyte ions and solvent molecules. The hydrogen bonding in PC molecules and the imidazolium ring in$[EMIM]^+$ cation increases the dissociation degree of ionic liquid led to faster redox reaction and higher capacitance values. Therefore, the coexistence of solvent molecules and ions inside the double layer (inner Helmholtz plane) influences the composition and structural characteristics under an electric field.[89] While at low potential, the inner layer is concentrated with nonpolar functional groups of the anions and cations, corresponding to the minimum of capacitance profile (close to the point of zero charge), with increasing potential the electrostatic

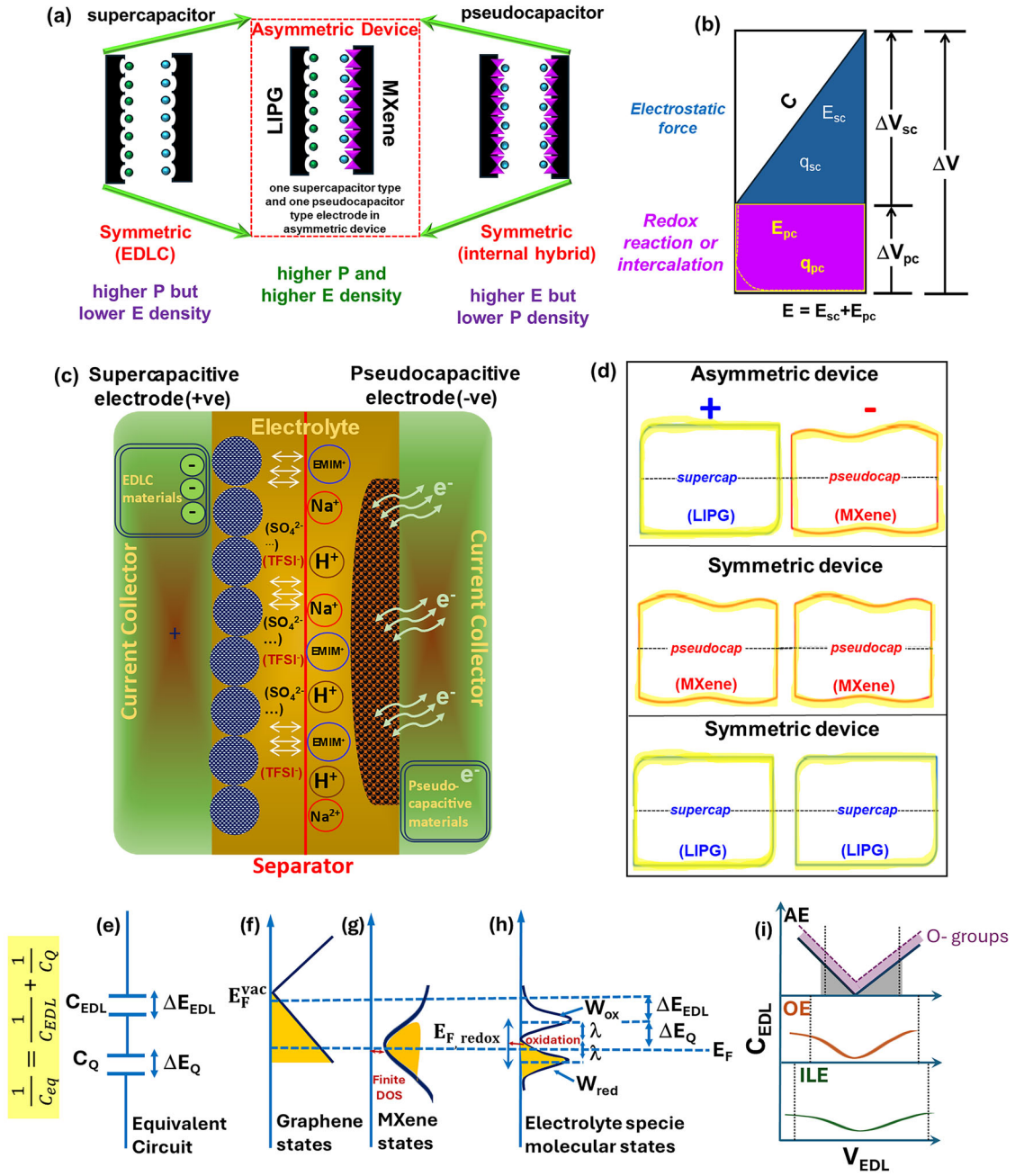

Figure 8. Schematics of hybridization, energy distribution, energy storage mechanism, and proposed energy level interfacial alignment under aqueous electrolyte. a) Single electrode systems (supercapacitor and pseudocapacitor) and their combination forming an asymmetric device with an expected high energy and power density. b) Corresponding charge-potential profile and c) energy storage mechanistic description and device structure for asymmetric supercapacitive–pseudocapacitive electrodes device. d) Representative material combinations for asymmetric (MXene/LIPG) and symmetric (MXene//MXene) devices. e) The total capacitance of asymmetric device at electrode/electrolyte interface. f,g) Density and occupation of states in the uncharged/un-electrified interface for LIPG and MXene. h) The Gaussian distribution and occupation of electrolyte molecular states in solution. i) Schematic of the anticipated double-layer capacitance (C_{EDL}) of classic ("V" shape) and oxygenated 2D layers in aqueous electrolyte (increased defect density) and how it changes under OE ("crescent" shape) and ILE ("camel" shape) environments with operating potential window (V_{EDL}).

interaction of polar/charged functional groups with the electrode surface compete leading to stereochemical ion rearrangement that increases the inner-layer charge density and results in higher capacitance. Figure 8 (panels e–h) displays a grand scheme of energy band alignment of electrodes and electrolyte structure. Experimental results and theory indicated that the total interfacial capacitance is associated with the relative contribution of differential electrochemical double-layer capacitance (C_{EDL}) and the space charge or quantum capacitance (C_Q), the latter often overlooked in the reports while discussing the supercapacitors

partly because they are determined from complex theoretical calculations. Thus, the total interfacial capacitance (C_{Total}) governed by the cumulative effect of C_Q and C_{EDL} is represented as two capacitances connected in series: $1/C_{Total} = I/C_{EDL} + 1/C_Q$, as in Figure 8e. Additionally, Figure 8f–h shows uncharged or non-electrified energy states and the distribution of electrolyte species in solution where the peak represents the oxidized (*unoccupied*) and reduced (*occupied*) state. The Fermi level of graphene i.e., horizontal dashed line shift relative to its vacuum level upon contact with an electrolyte ($E_{F,electrolyte}$). It is likely that during voltammetry experiments, cumulative shifts occur affecting electrode kinetics and specific capacitance as has been realized. Finally, the camel-shaped capacitance profile determined with ionic liquid electrolyte for layered materials is in contrast with the typical "V" shaped profile with an aqueous and crescent-shaped profile for organic electrolyte shown in Figure 8i that results from the electric-field-induced stereochemical rearrangement of ion structure within the inner Helmholtz layer closest to the electrode interface mentioned above. From the charging mechanisms of ionic liquid at the electrode with finite and sufficient DoS near the Fermi level (as in MXene and LIPG, see Figure 8e–i), the hydrophobic[EMIM][TFSI] drives the water molecules toward the electrode surface and limiting the potential window to 2.5 V (≈3.0 V) observed in our study. For enhanced cell voltage, this subsection analyzed ASCs analytically through electrochemical performance metrics. A symmetric system having both positive and negative electrodes of the same material and aqueous electrolyte, the specific energy storage capacity will be the same as that of a single capacitor-type electrode given by:[11]

$$E_{sym} = \frac{1}{2} q_s.\Delta V_{max},\ ED_{sym} = \frac{1}{2}\frac{q_s.\Delta V_{max}}{m_s}.\ \frac{1}{3600\ s} \tag{15}$$

On the other hand, for an asymmetric device having different positive (supercapacitive) and negative (pseudocapacitive/redox) electrodes, they have different charge storage and energy management capabilities ascribed to stronger adsorption force of electrolyte-anion than that of electrolyte−cation during charging process as the electrostatic potential increases. It is critical to use a higher operating potential at the initial stages of charging with capacitor type electrode results in a faster process. It is presumed that the redox reaction kinetic rate of a pseudocapacitive electrode is sluggish in comparison to electrostatic charge storage of supercapacitor type electrode with aqueous electrolyte in an actual system, *albeit* fast enough to operate as a capacitor type counter electrode. Therefore, the total energy storage capacity and energy density are additive such that:

$$E_{asym} = \frac{1}{2}.q_{asym}.\Delta V_{cap} + \frac{1}{2}\ q_{asym}.\Delta V_{pseudocap},\ E_{asym} > E_{sym} \tag{16}$$

where q_{asym} is the charge stored in both the electrodes and asymmetric capacitor system and ΔV_{cap} and $\Delta V_{pseudocap}$ are the working potential range of capacitor-and pseudocapacitor-type electrodes, respectively. Correspondingly, the gravimetric energy density (ED) follows as:

$$\begin{aligned} ED_{sym} &= \frac{1}{2}.\frac{q_{sym}.\Delta V_{max}}{m_{sym}};\ ED_{asym} = \frac{E_{cap}+E_{pseudocap}}{m_{cap}+m_{pseudocap}}.\frac{1}{3600s} \\ &= \frac{q_{asym}.\Delta V_{cap}+q_{asym}.\Delta V_{pseudocap}}{m_{cap}+m_{batpseudocap}}.\frac{1}{3600s} \\ &= \frac{1}{2}.\frac{q_{asym}}{m_{asym}}\left(\Delta V_{cap} + \Delta V_{pseudocap}\right).\frac{1}{3600s} \end{aligned} \tag{17}$$

It is apparent the ED of an asymmetric device is larger than symmetric capacitor device for aqueous as well as other electrolytes. The specific power density (PD) for a single capacitor electrode (PD_1), symmetric (PD_{sym}) and asymmetric energy device (PD_{asym}) systems with aqueous electrolyte can be determined from the following equations:

$$PD_1 = \frac{I_{max}.\Delta V_{max}}{m_1};\ PD_{sym} = \frac{I_{max}.\Delta V_{max}}{m_{sym}} \tag{18}$$

$$PD_{asym} = \frac{I_{max}.\Delta V_{max}}{m_{asym}} = \left(\frac{1-k_1}{1-k_2}\right).PD_1 \tag{19}$$

where $k_1 = \frac{m_{pseudocap}}{m_{asym}}$ $(0 < k_1 < 1)$ and $k_2 = \frac{\Delta V_{pseudocap}}{\Delta V_{max}}$ $(0 < k_2 < 1)$ are the ratio of electrode active mass and operating potential, respectively. It clearly indicates that the asymmetric energy devices give an advantage of better electrochemical performance (calculated to be twice in compliance with experimental values) compared with a symmetric system in aqueous electrolyte under $k_1 < k_2$ condition. Based on these model considerations and previous studies it becomes apparent that asymmetric supercapacitors under organic and ionic liquid electrolytes with larger ΔV_{max} exhibit higher performance than those of the same system with an aqueous electrolyte.[9,90] From a practical standpoint, the electrochemical performance of MXene-based asymmetric supercapacitors was derived from the overall mass and total volume of negative and positive electrodes. Beyond half cells with MXene and LIPG electrodes, the mass ratio of positive to negative electrode was set at ≈3:1 or 4:1, based on the capacities of both electrodes with overcapacity of LIPG positive electrode to allow potential stability for negative MXene electrode. The interdigitated coplanar electrode setup allows for fast electrolyte ion diffusion between 2D sheets when compared to cofacial sandwich geometry (that is, electrodes being stacked sequentially with a glass fiber separator). On design consideration, the areal ratio defined as $r = \frac{A_1}{A_2} = \frac{mL_1w_1}{nL_2w_2}$, $m = n, n+1$, where L, lengths, W, widths, and n and m, number of digits and thus, the six parameters can be finely tuned to perform areal balancing. Likewise, charge balance and minimization of ohmic losses are other strategies to maximize energy and power densities, and the literature is devoid of such intensive investigations reported in this work. Charge balancing is an optimization procedure to let anodes (negative), and cathodes (positive) operate in their full potential window, allowing the device to obtain the maximum energy density. With mass and areal or volume optimization of positive (designated 1) to negative electrode (designated 2) i.e., $r = C_2.m_1/C_1.m_2$), the cell voltage can be reached up to 1.6 V in aqueous media and can be cycled for hundreds and thousands (i.e., >50 000 cycles) to million (i.e., >200 000 cycles) cycles. Finally, since the energy device performance is strongly associated

with molecular level ion adsorption (charging)/desorption (discharging) at the electrode surface, we continued to advance our understanding relating to structural organization and dynamic interfacial processes.

3. Conclusion

In summary, we demonstrated facile fabrication strategies of asymmetric supercapacitors (ASCs) at the microscale comprising pseudocapacitive MXene as negative and supercapacitive LIPG as positive electrodes configured in lateral (coplanar) and sandwich (cofacial) architectures that are commercially feasible. Notably, these innovative devices are scalable, flexible, current collectors and binder–free, which operates successfully at larger potential windows. A fair assessment of electrochemical performance under different electrolyte compositions (aqueous, polymer gel, and ionic liquid) with a view to enhanced specific energy density comparable to rechargeable secondary batteries facilitated by hybridized redox chemistry of disparate electrode charging mechanisms used as a benchmark for long duration energy storage devices. This work also revealed the capability of MXene electrode to operate at high cathodic voltages in aqueous electrolytes besides LIPG electrode presenting a reasonable capacity (≈0.062 kWh kg^{-1}) than commercial activated carbons (0.040 kWh kg^{-1}). The true performance metrics are presented by considering the mass/volume of each cell component and the electrolyte yielding the highest specific energy recorded for the ILE-sandwich device, while the highest power density was characteristic with the AE-sandwich device followed by intermediate values for the OE-lateral device. The MXene-based ASCs bridged the gap between conventional batteries and electrochemical capacitors maintaining performance over thousands of cycles and exhibiting high specific energy for ILE followed by OE and AE environments. At a fundamental level, the electrode-electrolyte interface is a complex interplay of hydration/solvation and intercalation energies as well as stereochemical configurations of anions and cations for OE and ILE that give rise to short-range intermolecular forces between ions themselves and with solvent molecules. The qualified pseudocapacitive MXene exhibited strong faradaic reactions at/near surfaces, while EDLC behavior of LIPG over a long range of potential offered high power density, and with these considerations, we defied expectations while unlocking possibilities of the energy storage in one asymmetric device. The mechanistic aspects underpin processes for a remarkably improved specific energy density that offered a potential strategy to promote cleaner and safer energy future toward generation-II electrochemical energy storage systems for microscale portable electronics, automotive, defense, and space (*e.g.*, advanced small satellites) applications.

4. Experimental Section

Synthesis of LIPG and $Ti_3C_2T_x$ (MXene), Preparation Of Electrolytes, and Fabrication Of Electrodes Assembly.—Synthesis of LIPG and MXene: Kapton PI polymer sheets ≈100 microns thick used in this work were purchased commercially from Cole Palmer (Type HN film, CatNo. WZ-08277-86, UK). They were used as received with gentle cleaning of dust particles. Laser scribing on the PI sheet was conducted with a pulsed CO_2 laser of 10.6 µm wavelength with a pulse duration of ≈50 ms (Model Desktop 3D Laser Printer, Model gweike cloud RF-Laser cutter, and engraver, Shandong, China). The beam size was ≈150 µm giving an estimate of interlayer or 1-pass distance. Laser power was 12%–17% of full laser power of 40 W. The laser system offers an option of controlling the scan rates from 20 to 500 mm s^{-1} and a scanning option (raster versus snake). The laser system also provides an option of setting the pulses per inch or DPI (dots per inch). Other than as specifically stated, the scan rates of 140–170 mm s^{-1} with the snake option were used for all experiments with comparable results. As for MXene ($Ti_3C_2T_x$) samples, they were prepared following the synthesis of Ti_3AlC_2 (MAX) phase as the first step.[81] Briefly, the submicron Ti_3AlC_2 grains were prepared by a molten salt method using elemental powders of Ti (99%, 325 mesh), Al (99%, 200 mesh), and carbon black (99%, primary particles size: 60 nm) in a molar ratio of 3:1.1:1.8 along with the reaction medium of mixed salts composed of equal proportion NaCl and KCl (= 50:50 mol%). The mixture was mixed for 12 h with agate balls and absolute alcohol in an agate jar, followed by drying at 60 °C for 8 h in air. The homogenized mixture was then heated in a tube furnace in a flowing Ar atmosphere. Finally, the sample was naturally cooled down to room temperature. Then, Ti_3AlC_2 was obtained by washing the mixture of Ti_3AlC_2 and salts with water several times. MXene was synthesized by etching Al species using the HCl/LiF route. In the second step, the as-prepared Ti_3AlC_2 MAX phase particles (1.0 g) pulverized from the monolith and immersed in 40 mL of fluoride-based salt etchant (3.2 g of LiF dissolved in 40 mL of 12 M HCl, forming HF in situ), heated at 45 °C for 24 h until no bubbles generated. The resulting particulate suspension was washed with DI water for m cycles to remove the excess acid and salt. They were also separated by vacuum filtration with a porous membrane filter (0.22 µm pore size) and washed with deionized water until the pH value of the supernatant was higher than 4. The final suspension was filtrated and freeze–dried for 72 h followed by mild heating at 60 °C in Ar gas to produce MXene ($Ti_3C_2T_x$) flakes. All the sample vials were stored in the refrigerator to suppress oxidation and environmental degradation. The fresh MXene could be reversibly redispersed into the homogeneous aqueous solution through light ultrasonication in DI water. After redispersing, MXene was disentangled into monolayered platelets, with the flake morphology and thickness quite like those of fresh MXene dispersion, and used as ink.

Synthesis of LIPG and $Ti_3C_2T_x$ (MXene), Preparation of Electrolytes, and Fabrication of Electrode Assembly.—Preparation of Different Electrolyte Composition: Aqueous electrolyte (AE) was prepared by dissolving 7.1g sodium sulfate (Na_2SO_4) in 100 mL DI water to prepare 0.5M Na_2SO_4 solution and it was used with Argon gas used for deoxygenation. A 2.5mM[$K_3/_4Fe(CN)_6$] redox probe with0.5M Na_2SO_4 base electrolyte was also used to analyze the LIPG electrode surface kinetics. The gel electrolyte of PVA was prepared following the reported work.[91] For organic electrolyte (OE), 1g PVA (Alfa AEsar, 98%) was dissolved in 20 mL DI water at 86°C for 3–4 h at which the transparent gel was achieved. Following that, 2g (1.68 mL) of concentrated sulfuric acid 1M H_2SO_4 (Alfa AEsar) was added to 20wt.% PVA gel and stirred for 40 min. to obtain 1M PVA/H_2SO_4 as polymer gel solid-state electrolyte. Ionic liquid electrolyte[EMIM][TFSI] (1-Ethyl-3-methylimidazolium bis(trifluoromethylsulfonyl)imide, >98%) was purchased commercially (Sigma-Aldrich, USA) and mixed with PC (Propylene Carbonate anhydrous, 99.7%, Sigma–Aldrich) in 70/30 *w/w* ratio to decrease viscosity of ionic liquid without compromising its ionic conductivity (≈20 mS cm^{-1}) used for conduction. It was noted that the OE (PVA/H_2SO_4) and ILE ([EMIM][TFS]/PC) have higher finite solution resistance as compared with AE (0.5 M Na_2SO_4) electrolytes. All the chemicals were purchased from Alfa AEsar and were used as-is without further purification.

Synthesis of LIPG and $Ti_3C_2T_x$ (MXene), Preparation of Electrolytes, and Fabrication of Electrodes Assembly.—Fabrication of Various Electrodes Assembly: LIPG facilitated the way forward producing maskless patternable, and controlled formation of flexible interdigitated lateral (coplanar) configuration devices significant for maximizing the performance, in contrast to time-consuming photolithography and multistep processing. To prepare symmetric and asymmetric planar electrodes-assembly, the first LIPG was directly written on PI using the computer-controlled predesigned interdigitated electrode CAD files (LightBurn Beta Software, *ver.* 0.4.06)„ which serves as the active electrodes in this study. The typical dimensions of the symmetric LIPG interdigitated electrode fingers were 1.5x0.2 mm^2, and

with 11 fingers, the total area exposed to electrolyte was ≈3.3 mm^2 for symmetric LIPG, and for symmetric MXene (MXene//MXene) electrodes were 1.5x0.4 mm^2, and with 12 fingers, the total area exposed to electrolyte was ≈7.2 mm^2. Therefore, for MXene-based asymmetric lateral devices, the total area was equal to 3.6+1.6 = 5.2 mm^2 in which the flakes or freeze–dried MXene 'cakes' were redispersed (5 mg mL^{-1} concentration) in water by ultrasonication appeared as ink to prepare electrode films using spray coat or drop cast methods. A razor blade or sharp edged knife was passed between the electrodes to avoid short circuits after drying in air. The thin copper tape strips were used alongside each of the electrodes with no contact with the electrolyte used (*e.g.*, positive LIPG and negative MXene connection). The final symmetric and asymmetric interdigitated devices were obtained as in Figure 2. For instance, the devices were soaked in AE and ILE for a few hours and OE (PVA/H_2SO_4) gel electrolyte was dropped cast onto the lateral configuration devices and left them dry overnight at room temperature in air. To prepare asymmetric electrodes for sandwich (cofacial) configuration, while LIPG of circular patterned films on PI was transferred to a thin Al disk of similar dimension by dry transfer method, MXene was drop casted on Al disk as a current carrier and the overall exposed geometric area was equal to 8.85 mm^2, dimensions were like planar configuration devices and comparable to microscale supercapacitors (MSCs). In addition, since the thickness of the electrodes used in this study was a micrometer or smaller dimension, they were assigned as micro-supercapacitors. The mass loading of active electrode was controlled materials and kept at ≈1mg (LIPG)−5mg (MXene). The electrode masses were calculated to be 600 µg cm^{-2} (or 0.6 mg cm^{-2}), 800 µg cm^{-2} (or 0.8 mg cm^{-2}), and 400 µg cm^{-2} (or 0.4 mg cm^{-2}) for LIPG//LIPG, MXene//MXene, and MXene//LIPG, respectively. The lateral and sandwich-configured symmetric electrochemical supercapacitor devices were also prepared for comparison.

Characterization—Surface Morphology and Microstructure: All the electrode samples were characterized using complimentary analytical techniques to reveal surface morphology, microstructure, and lattice vibration properties of electrodes. Scanning electron microscopy (SEM) images were taken with an instrument (Model Prisma E Thermo Fisher Scientific, USA) operating at a primary electron acceleration voltage 15 kV at a constant current 45 µA in secondary electron imaging mode with a LaB_6 filament. For nanoscale morphology, transmission electron microscopy (TEM) was used to which a few flakes were distributed onto commercial carbon coated with 2% collodion solution (Sigma Aldrich) 300 mesh grids (Agar) and analyzed with transmission electron microscope (Model Tecnai Spirit BioTWIN) operating at 120kV and 1 nA from LaB_6 gun with a Be specimen holder and with AMT 8 Mpixel cooled camera. The structure of the obtained material was analyzed with an X-ray diffractometer Philips X'pert PRO with Anton Parr HTK-1000 camera and CuK_α radiation (λ = 1.54 Å) in the range of $2\theta = 5°–70°$. The characterizations were conducted directly on electrode films. Lattice vibrational spectra were recorded using a micro-Raman spectrometer with LEICA setup (Model InVia Renishaw *plc*, Hoffman Estates, IL, USA) equipped with LEICA setup and Ar^+ laser providing excitation wavelength λ_L = 514 nm (E_L = 2.41 eV), 1800 lines mm^{-1} grating yielding spectral resolution of 1 cm^{-1}. The reflected light was filtered using an edge filter to remove the laser excitation cutting at ≈100 cm^{-1}. The scattered light from the sample was collected in backscattering geometry with an objective lens of 50x providing a spot size of ≈1–2 µm, and the laser power on the sample was maintained between < 0.1–0.5 mW (10 %) to prevent photo-thermal degradation. The Raman spectra was acquired for 90–120 s dwell time to maximize the throughput signal. Raman spectra ranged in between 100–1000 cm^{-1}. Each sample was analyzed at four randomly selected points, and the spectra were averaged from these measurements. The electrical conductivity of electrode films was measured using a four-point probe with a distance of 1 mm which was connected to a Keithley 2400 source meter with a detection limit 1GΩ (Keithley, Cleveland, OH, USA) and calculated room temperature electrical conductivity (σ_{dc}). The surface chemical composition of the LIPG surface was performed using an Argus Omicron NanoTechnology X-ray photoelectron spectrometer (XPS). XPS spectroscopy was performed on the sample after electrical measurements. The analysis was performed at room temperature with a base pressure below 1.1 × 10^{-9} mbar. The photoelectrons were excited by an MgKα X-ray anode. An Omicron Argus hemispherical electron analyzer with a round aperture of 4 mm was used. Measurements were taken in a constant analyzer energy (CAE) mode with pass energy equal to 50 eV. To remove contamination and oxides, the surface was etched with Ar ions before the measurement. All the survey spectra were recorded in 0.5 eV step size with a pass energy of 140 eV. Elemental C1s spectra were recorded in 0.1 eV step sizes with a pass energy of 26 eV. All the spectra were corrected using C1s peaks (284.5 eV) as a reference. The data was processed in CasaXPS

Characterization—Electrochemical Properties: The electrochemical measurements were performed using a potentiostat-galvanostat (VMP-300, Bio-Logic, France), controlled by EC-Lab software (v11.52). Cyclic voltammetry (CV) and electrochemical impedance spectroscopy (EIS) were conducted in two-electrode Swagelok cell configuration with LIPG and MXene as the working electrodes, and in three-electrode configurations with Ag/AgCl/3M KCl as the reference electrode. The geometric surface area of the electrode immersed in the electrolyte was mentioned above. Before the electrochemical measurements, the solutions were typically deoxygenated with Ar gas to ensure full diffusion of ions onto surfaces of LIPG electrodes, they were soaked in electrolyte for 3–4 h. For better electrical connection, silver paint was also applied on the electrode, and it was extended with conductive copper tape and then connected to the electrochemical workstation. To protect the contact pads from the electrolyte, Kapton tape was used. The CV experiments were conducted at scan rates of 5–500 mV s^{-1} and the potential range was from 0.8 to +2.5 V *versus* the reference electrode depending upon the electrolyte type. The *ac* EIS experiment was conducted at open circuit potential (OCP), with an ac voltage perturbation amplitude of 10 mV, and in the frequency range of 2 × 10^5 (200 kHz) to 1 × 10^{-2} Hz (10 mHz), 10 points per frequency decade. An equilibrium state for OCP was confirmed by the attainment of a stable value occurring within 20 to 45 min. The galvanostatic charging-dischargeing (GCD) measurements were also performed with current densities from 0.12 to 2.4 A g^{-1} for thousands of cycles ran for at least five days to determine capacitance retention and Coulombic efficiency. All the experimental measurements recorded at room temperature 25 °C were repeated five times (sample size n = 5) giving rise to reproducibility within 5–8% (standard error mean).

Supporting Information

Supporting Information is available from the Wiley Online Library or from the author.

Acknowledgements

The corresponding author (S.G.) is grateful for the financial support for these studies from Gdansk University of Technology by the DEC-37/2022/IDUB/1.1/NOBELIUM grant under IDUB Nobelium Joining Gdańsk Tech Research Community-'Excellence Initiative-Research University' program. The authors also acknowledge initial technical assistance from F. Skiba and P. Jakóbczyk. [Correction added on April 7, 2025, after first online publication: Caption figure 2 and 3 has been swapped.]

Conflict of Interest

The authors declare no conflict of interest.

Author Contributions

S.G. dealt with conceptualization, resources, visualization, investigation, writing the original draft, editing and supervision. M.N. dealt with the resources, visualization, writing and editing. M.S. dealt with the resources, visualization, writing and editing. J.B.J. dealt with resources, visualization, writing and editing. R.B. dealt with resources, writing, editing and supervision. S.Y. dealt with resources, investigation, writing and editing.

Data Availability Statement

The data that support the findings of this study are available on request from the corresponding author. The data are not publicly available due to privacy or ethical restrictions.

Keywords

asymmetric supercapacitors, electrode/electrolyte interfaces, laser-induced graphene, MXene, performance considerations

Received: February 21, 2025
Revised: March 16, 2025
Published online:

[1] O. Edenhofer, R. P. Madruga, Y. Sokona, Renewable energy sources and climate change mitigation: Summary for policymakers and technical summary, International Panel of climate change, IPCC Eds., Cambridge University Press, Cambridge, England, **2012**.
[2] B. E. Conway, *Electrochemical Supercapacitor: Scientific Fundamentals and Technological Applications*, Plenum, New York, **1999**.
[3] S. Gupta, S. B. Carrizosa, *Appl. Phys. Lett.* **2016**, *109*, 243903.
[4] T. M. Gür, *MRS Bull.* **2021**, *46*, 1153.
[5] G. Crabtree, N. Lewis, *Phys. Today* **2007**, *60*, 37.
[6] E. C. Choi, Y. Luo, A. Reed, G. Whang, B. Dunn, BP Statistical Review of World energy **2022**.
[7] N. Wu, X. Bai, D. Pan, B. Dong, R. Wei, N. Naik, R. R. Patil, Z. Guo, *Adv. Mater. Interfaces* **2020**, *8*, 2001710.
[8] C. Zhao, W. Zheng, *Front. Energy Res.* **2015**, *3*, 23.
[9] S. Gupta, S. B. Carrizosa, B. Aberg, *Sci. Rep.* **2024**, *14*, 29277.
[10] H. S. Choi, C. R. Park, *J. Power Sources* **2014**, *259*, 1.
[11] J. B. Goodenough, Y. Kim, *Chem. Mater.* **2010**, *22*, 587.
[12] E. Frackowiak, M. Meller, J. Menzel, D. Gastol, K. Eric, *Faraday Discuss.* **2014**, *172*, 179.
[13] S. Gupta S, M. vanMeveren, J. Jasinski, *J. Electron Mater.* **2015**, *44*, 62.
[14] S. Gupta, M. M. vanMeveren, J. Jasinski, *Int. J. Electrochem. Sci.* **2015**, *10*, 10272.
[15] S. Gupta, B. Aberg, S. B. Carrizosa, N. Dimakis, *Materials* **2016**, *9*, 615.
[16] M. Winter, R. Brodd, *Chem. Rev.* **2004**, *104*, 4245.
[17] J. Miller, P. Simon, *Science* **2008**, *321*, 651.
[18] A. Burke, *J. Power Sources* **2000**, *91*, 37.
[19] M. D. Stoller, S. J. Park, Y. W. Zhu, J. H. An, R. S. Ruoff, *Nano Lett.* **2008**, *8*, 3498.
[20] S. Gupta, B. Evans, A. Henson, *Desalin. Water Treat.* **2019**, *162*, 97.
[21] S. Gupta, B. Evans, *J. Mater. Sci.* **2023**, *58*, 11198.
[22] S. Gupta, S. B. Carrizosa, B. McDonald, J. Jasinski, N. Dimakis, *J. Mater. Res.* **2016**, *32*, 301.
[23] A. Balducci, D. Belanger, T. Brousse, J. W. Long, W. Sugimoto, *J. Electrochem. Soc.* **2017**, *164*, A1487.
[24] T. Christen, M. W. Carlen, *J. Power Sources* **2000**, *91*, 210.
[25] M. Pumera, *Energy Environ. Sci.* **2011**, *4*, 668.
[26] X. Li, Z. Zhao, Y. Deng, D. Ouyang, X. Yang, S. Chen, P. Liu, *Sci. Rep.* **2024**, *14*, 16751.
[27] Y. Huang, J. Luo, J. Peng, M. Shi, X. Li, B. Chang, *J. Energy Storage* **2020**, *27*, 101075.
[28] A. K. Geim, K. S. Novoselov, *Nat. Mater.* **2007**, *6*, 183.
[29] S. Gupta, N. Dimakis, *J. Appl. Phys.* **2016**, *130*, 084902.
[30] C. Choi, Y. Luo, A. Reed, G. Whang, B. Dunn, *Chem. Mater.* **2024**, *36*, 11738.
[31] T. Nakajima, A. Mabuchi, R. Hagiwara, *Carbon* **1988**, *26*, 357.
[32] W. Schölz, H. P. Z. Boehm, *Zeitschrift für anorganische und allgemeine Chemie* **1969**, *369*, 327.
[33] Y. Shao, J. Wang, H. Wu, J. Liu, I. A. Aksay, Y. Lin, *Electroanal.* **2010**, *22*, 1027.
[34] E. Luais, M. Boujtita, A. Gohier, A. Tailleur, S. Casimirius, M. A. Djouadi, A. Granier, P. Y. Tessier, *Appl. Phys. Lett.* **2009**, *95*, 014104.
[35] S. Gupta, R. Meek, *Appl. Phys. A* **2020**, *120*, 704.
[36] S. Gupta, A. Sharits, J. Boeckl, *J. Appl. Phys.* **2023**, *134*, 074902
[37] S. Gupta, R. Meek, B. Evans, *J. Appl. Phys.* **2018**, *124*, 124034.
[38] J. Lin, Z. Peng, Y. Liu, F. R. Zepeda, R. Ye, E. L. G. Samuel, M. Jose Yacaman, B. I. Yakobson, J. M. Tour, *Nat. Commun.* **2014**, *5*, 5714.
[39] K. Avinash, F. Patolsky, *Mater. Today* **2023**, *70*, 104.
[40] M. F. El-Kady, R. B. Kaner, *ACS Nano* **2014**, *8*, 8725.
[41] A. Velasco, Y. K. Ryu, A. Hamada, A. de Andrés, F. Calle, J. Martinez, *Nanomaterials* **2023**, *13*, 788.
[42] H. Wang, Z. Zhao, P. Liu, X. Guo, *Biosensors* **2022**, *12*, 55.
[43] M. G. Stanford, K. Yang, Y. Chyan, C. Kittrell, J. M. Tour, *ACS Nano* **2019**, *13*, 3474.
[44] S. Gupta, M. vanMeveren, J. Jasinski, *Int. J. Electrochem. Sci.* **2015**, *10*, 10272.
[45] L. Yanga, S. Cheng, X. Ji, Y. Jiang, J. Zhou, M. Liu, *J. Mater. Chem. A* **2015**, *3*, 7338.
[46] S. Gupta, S. B. Carrizosa, *AIP Adv.* **2018**, *8*, 065225.
[47] G. A. Snook, P. Kao, A. S. Best, *J. Power Sources* **2010**, *196*, 1.
[48] S. Gupta, C. Price, *Composites B: Engineering* **2016**, *105*, 46.
[49] M. A. Bissett, S. D. Worrall, I. A. Kinloch, R. A. W. Dryfe, *Electrochim. Acta* **2016**, *201*, 30.
[50] M. Acerce, D. Voiry, M. Chhowalla, *Nat. Nanotechnol.* **2015**, *10*, 313.
[51] L. Cao, S. Yang, W. Gao, Z. Liu, Y. Gong, L. Ma, G. Shi, S. Lei, Y. Zhang, S. Zhang, R. R. Vajtai, P. M. Ajayan, *Small* **2013**, *9*, 2905
[52] Z. Cao, R. Momen, S. Tao, D. Xiong, Z. Song, X. Xiao, W. Deng, H. Hou, S. Yasar, S. Altin, F. Bulut, G. Zou, X. Ji, *Nano-Micro Lett.* **2022**, *14*, 181.
[53] Q. Zhu, J. Li, P. Simon, B. Xu, *Energy Storage Mater.* **2021**, *35*, 630.
[54] S. Gupta, W. Ringo, M. Hu, X. Wang, *J. Electron. Mater.* **2020**, *49*, 4028.
[55] Y. Zhou, K. Maleski, B. Anasori, J. O. Thostenson, Y. Pang, Y. Feng, K. Zeng, C. B. Parker, S. Zauscher, Y. Gogotsi, J. T. Glass, C. Cao, *ACS Nano* **2020**, *14*, 3576.
[56] B. Pal, S. Yang, S. Ramesh, V. Thangadurai, R. Jose, *Nanoscale Adv* **2019**, *1*, 3807.
[57] T. Bhat, P. S. Patil, R. B. Rakhi, *J. Energy Storage* **2022**, *50*, 104222.
[58] C. Zhong, D. Sun, Y. Deng, W. Hu, J. Qiao, J. Zhang, *Electrolytes for Electrochemical Supercapacitors*, CRC Press, Boca Raton, FL, USA, **2016**.
[59] K. Fic, G. Lota, M. Meller, E. Frackowiak, *Energy Environ. Sci.* **2012**, *5*, 5842.
[60] S. Alipoori, S. Mazinani, S. H. Aboutalebi, F. Sharif, *J. Energy Storage* **2020**, *27*, 101072.
[61] M. Galiński, A. Lewandowski, I. Stępniak, Electrochim. Acta, *Ionic liquids as electrolytes* **2006**, *51*, 5567.
[62] A. Brandt, S. Pohlmann, A. Varzi, A. Balducci, S. Passerini, *MRS Bull.* **2013**, *38*, 554.
[63] S. Melchior, K. Raju, I. Ike, R. Erasmus, G. Kabongo, I. Sigalas, S. Iyuke, K. Ozoemena, *J. Electrochem. Soc.* **2018**, *165*, A501.
[64] N. A. Kyerematen, T. Brousse, D. Pech, *Nat. Nanotechnol.* **2017**, *12*, 7.
[65] T.-R. Cui, D. Li, T. Hirtz, W.-C. Shao, Z. B. Zhou, S.-R. Ji, T.-L. Ren, *Appl. Sci.* **2023**, *13*, 4688.
[66] S. G. Jo, R. Ramkumar, J. W. Lee, *ChemSusChem* **2024**, *17*, 202301146.
[67] T. Habib, X. Zhao, S. A. Shah, Y. Chen, W. Sun, H. An, J. L. Lutkenhaus, M. Radovic, M. J. Green, *Appl* **2019**, *3*, 8.
[68] I. R. Shein, A. L. Ivanovskii, *Micro Nano Lett* **2013**, *8*, 59.
[69] S. Gupta, A. Saxena, *J. Raman Spectroscopy* **2010**, *40*, 1127.
[70] K. Jurkiewicz, M. Pawlyta, D. Zygadło, A. Burian, *J. Mater. Sci.* **2018**, *53*, 3509.

[71] G. J. Brug, A. L. G. van den Eeden, M. Sluyters-Rehbach, J. H. Sluyters, *J. Electroana. Chem. Interf. Electrochem.* **1984**, *176*, 275.
[72] M. A. Pimenta, G. Dresselhaus, M. S. Dresselhaus, L. G. Cançado, A. Jorio, R. Saito, *Phys. Chem. Chem. Phys.* **2007**, *9*, 1276.
[73] E. P. Randviir, *Electrochim. Acta* **2018**, *286*, 179.
[74] E. Paek, A. J. Pak, K. E. Kweon, G. S. Hwang, *J. Phys. Chem. C* **2013**, *117*, 5610.
[75] C. Couly, M. Alhabeb, K. L. Van Aken, N. Kurra, L. Gomes, A. M. Navarro-Suárez, B. Anasori, H. N. Alshareef, Y. Gogotsi, *Adv. Electron. Mater.* **2018**, *4*, 1700339.
[76] B.-S. Shen, H. Wang, L.-J. Wu, R.-S. Guo, Q. Huang, X.-B. Yan, *Chinese Chem. Lett.* **2016**, *27*, 1586.
[77] Z. Niu, L. Zhang, L. Liu, B. Zhu, H. Dong, X. Chen, *Adv. Mater.* **2013**, *25*, 4035.
[78] J. Chen, Y. Han, X. Kong, X. Deng, H. J. Park, Y. Guo, S. Jin, Z. Qi, Z. Lee, Z. Qiao, R. S. Ruoff, H. Ji, *Angew. Chem.* **2016**, *128*, 14026.
[79] M. E. Orazem, B. Tribollet, *Electrochemical Impedance Spectroscopy*, John Wiley & Sons, Hoboken, NJ, **2008**.
[80] B. Hirschorn, M. E. Orazem, B. Tribollet, V. Vivier, I. Frateur, M. Musiani, *J. Electrochim. Soc.* **2010**, *157*, C458.
[81] Y. Guo, Z. Du, Z. Cao, B. Li, S. Yang, *Small Methods* **2023**, *7*, 2201559.
[82] M. E. Orazem, N. Pébère, B. Tribollet, *J. Electrochem. Soc.* **2006**, *153*, B129.
[83] J. N. Soderberg, A. C. Co, A. H. C. Sirk, V. I. Birss, *J. Phys. Chem. B* **2006**, *110*, 10401.
[84] C.-C. Liu, D.-S. Tsai, W.-H. Chung, K.-W. Li, K.-Y. Lee, Y.-S. Huang, *J. Power Sources* **2011**, *196*, 5761.
[85] K. Wang, W. Zou, B. Quan, A. Yu, H. Wu, P. Jiang, Z. Wei, *Adv. Energy Mater.* **2011**, *1*, 1068.
[86] N. P. Shetti, A. M. Soumen, B. Tejraj, M. Aminabhavi, A. Alodhay, S. Pandiaraj, *Energy Fuels* **2023**, *37*, 12541.
[87] J. H. Chae, K. C. Ng, G. Z. Chen, *Proc. Inst. Mech. Eng., Part A* **2010**, *224*, 479.
[88] Y.-J. Tu, J. G. McDaniel, *J. Phys. Chem. C* **2021**, *125*, 20204.
[89] M. Vijayakumar, B. Schwenzer, V. Shutthanandan, J. Z. Hu, J. Liu, I. A. Aksay, *Nano Energy* **2014**, *3*, 152.
[90] V. Khomenko, E. Raymundo-Pinero, F. Béguin, *J. Power Sources* **2008**, *177*, 643.
[91] L. Wang, H. Yang, X. Liu, R. Zeng, M. Li, Y. Huang, X. Hu, *Angew. Chem., Int. Ed.* **2017**, *56*, 1105.

